A modular field system for near-surface, vertical profiling of the atmospheric composition in harsh environments using cavity ring-down spectroscopy

Andrew W. Seidl[1], **Harald Sodemann**[1], **and Hans Christian Steen-Larsen**[1]

[1]Geophysical Institute and Bjerknes Centre for Climate Research, University of Bergen, Norway

Correspondence: Andrew W. Seidl (andrew.seidl@uib.no)

Abstract. Cavity ring-down spectroscopy (CRDS) has allowed for increasingly widespread, in-situ observations of trace gases, including the stable isotopic composition of water vapor. However, gathering observations in harsh environments still poses challenging, particularly in regard to observing the small-scale exchanges taking place between surface and atmosphere. It is especially important to resolve the vertical structure of these processes. We have designed the ISE-CUBE system as a modular CRDS deployment system for profiling stable water isotopes in the surface layer, specifically the lowermost $2\,\mathrm{m}$ above the surface. We tested the system during a two-week field campaign during Feb-March 2020 in Ny-Ålesund, Svalbard, Norway, with ambient temperatures down to $-30\,^{\circ}\mathrm{C}$. The system functioned suitably throughout the campaign, with field periods exhibiting only a marginal increase in isotopic measurement uncertainty ($30\,\%$) as compared to optimal laboratory operation. Over the $2\,\mathrm{m}$ profiling range, we have been able to measure and resolve gradients on the time and spatial scales needed in an Arctic environment.

1 Introduction

Understanding exchange processes between the atmosphere and surface is fundamental to constrain fluxes between reservoirs in the Earth System. There exist substantial knowledge gaps on these processes and their representation in models, especially at high latitudes and other cold environments (Wahl et al., 2021; Ritter et al., 2016). Near surface ($<2\,\mathrm{m}$) gradients of scalars can be strengthened significantly due to the stable stratification that often occurs in these regions (Jocher et al., 2012; Zeeman et al., 2015), which ultimately govern the fluxes of trace gases such as methane, carbon dioxide, and water vapor. In cold regions in particular, where ice and snow are prevalent, the quantification of the evaporation and condensation flux of water vapor requires multi-height, in-situ measurements. In this regard, the stable isotope composition of the water vapor is a valuable asset, as quantified by the heavy isotopologues, $\mathrm{HD^{16}O}$ (D=deuterium, $^{2}\mathrm{H}$) and $\mathrm{H_2^{18}O}$, as well as the rarer $\mathrm{H_2^{17}O}$. Hereby, the relative abundances of the stable water isotopes (isotopologues) (SWIs) impart information about phase changes, and thus the exchange between different reservoirs of the hydrological cycle.

Laser spectroscopy has enabled the continuous, high-resolution observation of the SWI composition in ambient air (Galewsky et al., 2016). In cavity ring-down spectroscopy (CRDS), the sample is guided through a measurement cavity with highly precise pressure and temperature control, while measuring the decay of a laser pulse in the infrared (Crosson et al., 2002; Gupta et al., 2009). Since the spectrometers are designed for set-up in a laboratory and similarly controlled environments, the in-situ measurement often relies on pre-existing infrastructure (Bonne et al., 2014; Galewsky et al., 2011) or tents (Steen-Larsen et al., 2013; Wahl et al., 2021).

At such pre-existing structures, water vapor isotopes are often continuously measured at one or several fixed-height inlets. Fixed height inlets must balance the number of lines with the robustness of their sampled gradient. Due to variations on many time scales, the inlet may not be at a height of interest for a particular measurement. In addition, over cold regions, turbulence in the surface layer often vanishes for extended periods (Mahrt, 2014), giving diffusional exchange processes a larger role. Due to kinetic fractionation of the SWIs, diffusional processes are particularly relevant for interpreting the measured water isotope signals in terms of surface properties (Thurnherr et al., 2021). While fixed-

height manifold systems are only partially able to resolve near-surface gradients, assessing the surface exchanges requires detailed profiling of the structure.

The characteristically dry ambient air in the high latitudes, and thus low absolute moisture concentration, limits the analytical precision of SWI measurements. Wall effects on the tubing can potentially further degrade measurement quality (Massman and Ibrom, 2008). Therefore, short, heated inlet lines limit potential interactions between water vapor and the inner walls of tubing. The use of short inlet lines also promotes a faster response of the CRDS analyzer, allowing for finer resolution of ambient signal variations in time and space. Munksgaard et al. (2011, 2012) applied a pragmatic approach, whereby the analyzer and accompanying equipment were housed inside a single plastic chest (on the order of $1\,\mathrm{m}^3$ in size) to facilitate their shipboard study of seawater along the tropical northeastern Australian coast. Despite the advantage of flexibility and low interference with the environment, a similar approach has not yet been attempted for the measurement of water vapor isotopes in the cold environmental conditions typical for high latitude winter.

Here we present a modular, in-situ profiling system, termed the ISE-CUBEs, that adequately protects the CRDS analyzer from the harsh Arctic environment during profiling of the near-surface layer. The ISE-CUBE system primarily consists of a stack of weather-proof plastic cases interconnected for ambient air sample transmission. These cases have a footprint of less than $1\,\mathrm{m}^2$ and a total volume of less than $0.5\,\mathrm{m}^3$. Attachment of a profiling sample arm allows for the detailed measurement of surface layer profiles in a $2\,\mathrm{m}$ range above the surface. An additional expansion module allows for the collection of water vapor in a cold trap system for later laboratory analysis, including $H_2^{17}O$. After a detailed description of the design principle and construction of the system, we evaluate its performance and the data quality based on measurements from a two-week field campaign at Ny-Ålesund, Svalbard, where the system encountered severe cold temperatures.

2 Measurement system design

The general aim of the ISE-CUBE system design was to enable ground-based, near-surface profiles of the vapor isotope composition. Installation and operation should be unaffected by weather conditions, in particular in regard to temperature and precipitation. The entire system should also induce minimal disturbance to the flow around the measurement site. Wall effects in the inlet should be minimized with short tubing lengths. Condensation need be prevented, to avoid measurement artifacts from fractionation and smoothed signals from memory effects. The system should be able to accommodate a cryogenic trapping module to collect discrete vapor samples for subsequent laboratory analysis. Based on these requirements, we designed a modular system that in its core was based on waterproof plastic containers, enabling setup by a single operator. We first give an overview of the overall arrangement of the measurement system, before describing each module in more detail.

2.1 Overall measurement system setup

The main body of the ISE-CUBE system consists of a stack of the two primary modules (Analyzer and Pump modules), in addition to the Cold Trap expansion module; a list giving specifics of individual components can be found in Table A1 (more details on system composition/construction can be found in Sect. 2 of the Supplemental Material). All three modules use the same plastic container (iM2875 Storm, Pelican Products Inc), allowing for stacking and fastening of the the stack, with a footprint of $0.38\,\mathrm{m}^2$ (see Figure 1). Each of the three modules is constantly ventilated with a $40\,\mathrm{m}^3\,\mathrm{h}^{-1}$ centrifugal fan. A plastic canvas can be placed over the stack for additional weather protection.

Gas transmission within the stack is via an inlet flow assembly (Figure 1, red dotted area) composed of approximately $70\,\mathrm{cm}$ of $1/4\,\mathrm{inch}$ stainless steel tubing (Swagelok Inc.), heated to $60\,^{\circ}\mathrm{C}$ with self-regulating heat trace cabling (Thermon Inc.). A main flow of approximately $9\,\mathrm{L\,min}^{-1}$ is drawn into the assembly (Figure 1b) with most going through the Cold Trapping module, using a vacuum pump in the Pump module (Figure 1b, "Inlet vacuum"). Analyzer flow is split off prior to entering the Cold Trapping module. A one-way check valve (6L-CW4S4, Swagelok Inc.) upstream of the analyzer inlet bulkhead (Figure 1b, "Check Valve") prevents reversal of the flow of sample air bound for the analyzer. The external vacuum pump of the CRDS analyzer (N920AP.29.18, KNF DAC GmbH) is also located in the Pump module (Figure 1b, "CRDS vacuum"). The inlet flow assembly also allows for connection to additional lengths of inlet tubing, such as the Profiling module which enables sampling at adjustable heights (see Sect. 2.4). We will now describe all four modules of the measurement system individually, beginning with the Analyzer and Pump as the core modules.

2.2 Analyzer module

We use a Picarro CRDS water isotope analyzer (L2130-i, Picarro Inc., USA) as the central element of the Analyzer module (Figure 1, middle container). The Analyzer module is lined with custom-fit Low Density Polyethylene (LDPE) foam padding to protect the analyzer. Some padding can be removed to increase ventilation flow for better temperature regulation, depending on ambient conditions during field operations. With a power draw of $\sim 100\,\mathrm{W}$ in steady state there is substantial heating from the analyzer. Therefore, adequate ventilation is required to keep the analyzer internal temperatures below around $50\,^{\circ}\mathrm{C}$, as prolonged exposure to higher

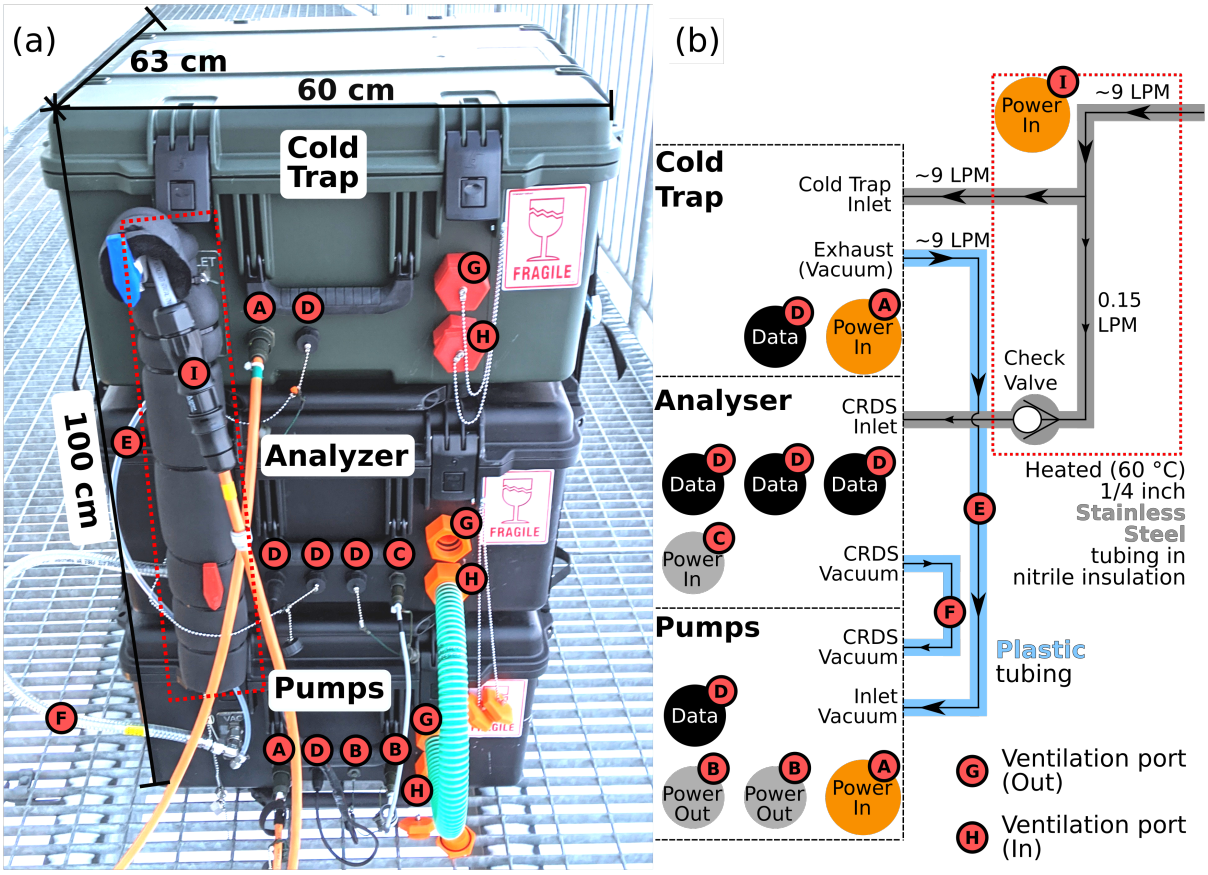

Figure 1. Overview of the ISE-CUBE system. (a) ISE-CUBEs in stacked configuration (from top to bottom): Cold Trap expansion module; Analyzer module; and Pump module. (b) Flow diagram for the entire ISE-CUBE system, including flow rates and connectors. A heated inlet assembly (red dotted area in both) connects the three modules for common gas transmission. See text for details.

temperatures (above 70 °C) can permanently damage electrical components

The analyzer computer can be controlled from an external laptop through a ethernet (RJ45) cable, or via USB-connected monitor and keyboard/mouse combination, with the "Data" connectors (Figure 1, D). The particular analyzer used here (Ser#: HIDS2254) is a custom modification of the standard L2130-i, which enables higher flow rates, similar to the analyzer described in Sodemann et al. (2017). The high flow rate is obtained by replacing the internal, constricting orifice (70 microns) needed for low-flow mode (typical flow rates $0.035\,\mathrm{L\,min^{-1}}$) with a standard $1/4\,\mathrm{inch}$ stainless steel section, in addition to using a stronger vacuum pump (N920AP.29.18, KNF DAC GmbH, Germany). High flow rates (about $0.15\,\mathrm{L\,min^{-1}}$) enable faster analyzer response and $4\,\mathrm{Hz}$ sampling, but they also cause more variable pressure inside the measurement cavity. The full impact of this particular configuration will be discussed in more detail below (Sect. 4.1). Sample air is guided from the exterior inlet bulkhead of the module into the analyzer via a $20\,\mathrm{cm}$ piece of flexible, $1/4\,\mathrm{inch}$ Polytetrafluoroethylene (PTFE) tubing. A similar length of $3/8\,\mathrm{inch}$, wire-reinforced, PVC tubing (K7160-06, Kuriyama of America Inc.) connects the vacuum port of the analyzer to the exterior bulkhead (Figure 1b, "CRDS Vacuum"). The vacuum and electrical bulkheads of the Analyzer module then connect to the Pump module (Figure 1, F: vacuum, B and C: electrical).

2.3 Pump module

The Pump module contains the pumps and additional components necessary for operation of the analyzer (Figure 1, bottom container). The Pump module is connected to the Analyzer module with a $3/8\,\mathrm{inch}$, wire-reinforced, PVC tubing (K7160-06, Kuriyama of America Inc.), providing the vacuum necessary for the analyzer (Figure 1b, "CRDS Vacuum"). The inlet vacuum pump (N022AN.18, KNF DAC GmbH, Germany) continuously flushes the inlet tubing, providing the main flow for both the analyzer and the Cold Trapping module (see Sect. 2.5). Additionally, a small 300 W Uninterruptible Power Supply (UPS) (EL500FR, Eaton) inside the module protects the analyzer from possible power fluctuations and short power breaks. This UPS also provides 12 V

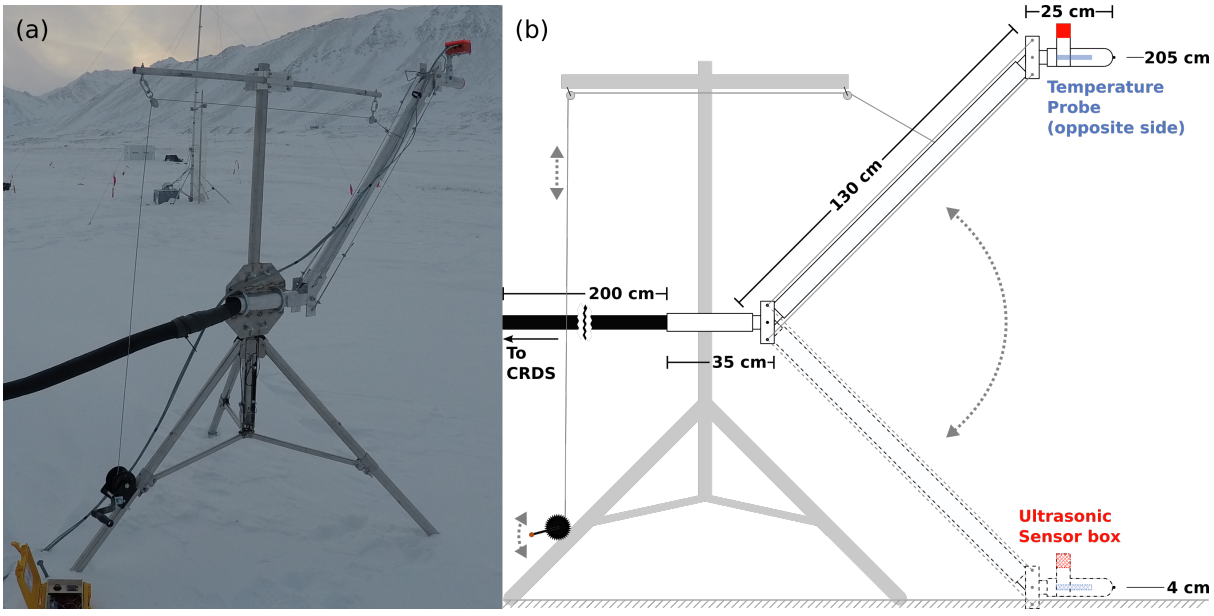

Figure 2. The Profiling module, with articulating arm. (a) Profiling module during field deployment. Inlet "head" in upper right of photo, with ultrasonic distance sensors encased in red plastic housing. Temperature sensor (not visible) located on opposite side of "head". Black winch in bottom left of photo controls inlet height via pulley system. Also visible in bottom left is the yellow case containing power supply and datalogger for temperature and distance sensors. Black tubing leading off to left connects to ISE-CUBE inlet. (b) Dimensional diagram for articulating arm.

power (via a 230 V AC-to-DC adaptor) for the Profiling module (Figure 1, B). All components in the Pump module are strapped to an aluminum support frame, which itself is firmly wedged between lid and bottom of the case, when the case is shut. Thereby, we could avoid drilling unnecessary mounting holes in the plastic case. Together, the Analyzer module and the Pump module are the two essential modules for in-situ isotopic measurement of water vapor. We will next describe the Profiling module, which enables high-resolution vertical profiling of the lowermost levels of the surface layer.

2.4 Profiling module

The Profiling module allows us to measure near-surface gradients of water vapor (atmospheric composition, more generally), as well as to investigate the exchange processes between surface and atmosphere. The Profiling module allows for the acquisition of vertical profiles of the ambient air at any height in a 2 m range (Figure 2). The lean design is expected to cause minimal flow disturbance at the measurement site. The module attaches to the inlet assembly (Figure 1, red dotted area) and consists of approximately 4 m of 1/4 inch stainless steel tubing (Swagelok Inc.), heated to 60 °C with self-regulating heat trace cable (Thermon Inc.), and surrounded with 2 cm thick foam nitrile insulation. Profiling capabilities are enabled by encasing the final 1.9 m of tubing in an aluminum articulating arm (Figure 2). The base of this arm is then attached to an aluminum mast and tripod with a custom-made steel mount (Supplemental Material). The tripod serves as the frame for a winch and pulley system to manually control the sampling height (Figure 2). Additional environmental parameters are acquired during profiling from a sensor package mounted on the "head" of the arm, near the air inlet. The height of the inlet is monitored by ultrasonic distance sensors (HC-SR04, SparkFun Elec.; Figure 2, red box). Air temperature at inlet sampling height is measured using a temperature probe (VMA324, Velleman; blue rectangle in Figure 2b). Both variables are logged onto an SD card via microcontroller (UNO, Arduino) housed inside a weatherproof container (Figure 2a, yellow case at lower left).

An alternate deployment frame was also custom-made for the profiling arm (Figure S1, Supplemental Material). This allowed us to mount the arm on an elevated platform and to reach downwards to the surface of the water (such as at the Fjord deployment site, Sect. 3.1). The arm mounts onto a ladder-like construction with steel U-bolts. Two right-triangular steel supports are mounted on their base legs, perpendicular to the face of the ladder, forming the main structure of the frame. Base and height legs of the triangular supports are approximately 1 m long. A wheel-and-axle crossbeam connect the two supports at the upper point of the height leg; this crossbeam supports the steel cable moving the arm. Any rung of the ladder construction can slide into two steel brackets which are bolted to the platform. While in "normal" orientation, the ladder construction and the head of the inlet arm would be horizontal. However, the entire frame could then tip forwards, pivoting about the secured

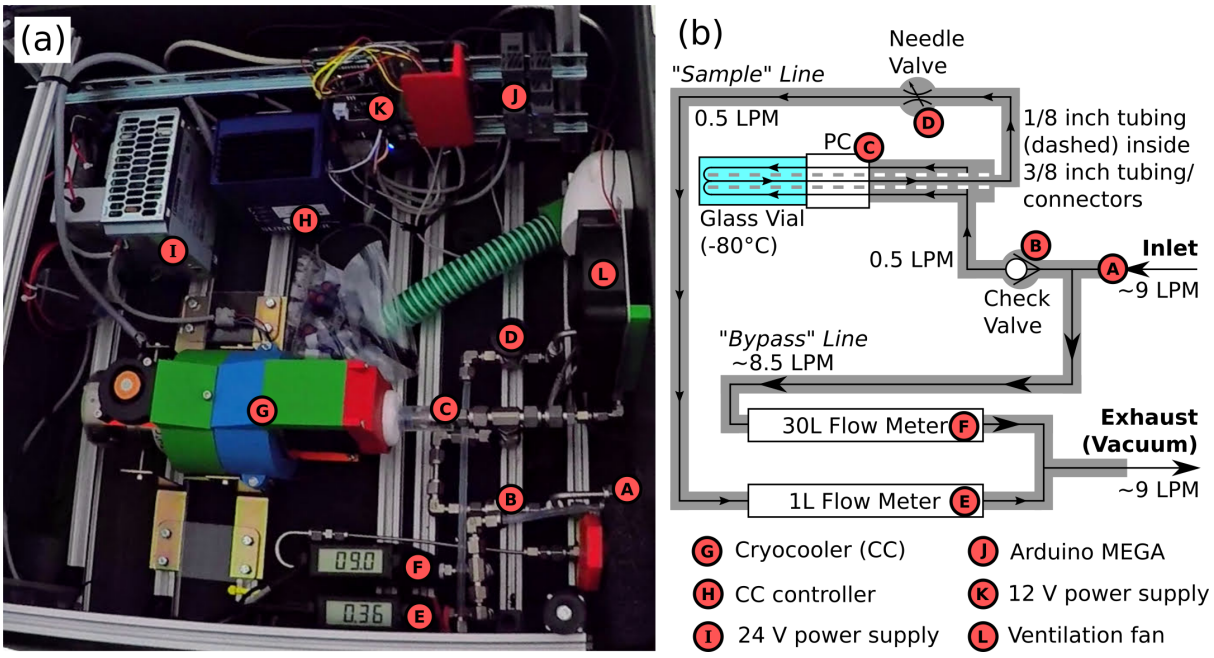

Figure 3. The Cold Trapping Module. (a) Interior of the module; cryocooler is surrounded by green, blue, and red plastic near photo center ("G"). (b) Flow diagram for the module. "PC" indicates placement of polycarbonate vial adapter. See text for details.

rung, with the ladder and inlet head both ending up vertical. This allowed us to make measurements 1.0 to 1.5 m further down at the Fjord site, though this did require an additional front-facing ultrasonic sensor. The fine-scale adjustment of the inlet head height was still possible with the winch and cable system, and was necessary to account for the tidal height changes of the seawater.

2.5 Cold Trapping expansion module

We included a cold trap module into the ISE-CUBE system, providing the ability to retrieve sample material from the field for subsequent laboratory analysis. This laboratory analysis could also include $\delta^{17}O$ for calculation of the ^{17}O-excess. Many commercially available Cold Trapping options involve the use of liquid cooling agents, such as ethanol or isopropyl alcohol. Peters and Yakir (2010) demonstrated the feasibility of collecting vapor samples with a Stirling cycle cryocooler as the cryogenic source of a cold trap. Due to the safe transportation and fast installation of such a cold trap, we adopted the basic design of Peters and Yakir (2010) for the ISE-CUBE cold trap expansion module.

The cryocooler migrates heat away from the tip of a cryogenic "finger" towards the body of the cryocooler, where the heat is radiated away through a radiator fin. By attaching this cryogenic finger to a thermally conducting mass (150 g of brass and aluminum) encircling a glass sampling vial, it directly cools the vial down to −80 °C. Incoming water vapor in sample air (Figure 3b, "Inlet") is routed through a combination of 3/8 inch stainless steel tubing and connectors, and is then introduced to the cooled glass collection vial, connected to the large bore tubing with a custom-made polycarbonate adapter ("PC" in Figure 3b). Upon entering the vial, the water vapor is rapidly cooled below its frost point, and it collects on the interior walls of the glass vial. The dried air exits the glass vial via a 1/8 inch length of stainless steel tubing, leading out of the end of the 3/8 inch tubing/connector combination. Finally, this 1/8 inch tubing is connected to the inlet vacuum pump (Figures 1b and 3b, "Exhaust (Vacuum)"), which provides the necessary flow for the Cold Trap. After the sampling period is complete, the flow is shut off with the needle valve (Figure 3, D), and the vial is manually removed, sealed, and stored until laboratory analysis, which can be done from the same vial. Also, the relatively small size of the setup easily fits within the standard ISE-CUBE container (Figure 1, top box).

We modified the original design of Peters and Yakir (2010) with regard to two aspects, namely the choice of cryocooler, and the flow configuration. Firstly, we opted for a more powerful cryocooler (L. Peters, personal communication, 20 March 2019), enabling faster and more consistent cooling of the sampling vial. Our chosen cryocooler (Cryotel MT, Sunpower Inc.; Figure 3, G) takes 5 to 6 minutes to reach −80 °C, at which temperature it has 23 W of cooling power. Secondly, as the system was designed to work in concert with the Analyzer and Pump modules, we utilized the inlet pump described in Sect. 2.3 to provide flow through the collection vial. Accomplishing this required the splitting of flow inside the Cold Trapping module into a "sample" and "bypass" line (Figure 3b). The "sample" line allowed incom-

ing, moist air into the glass collection vial, with flow regulation (approximately $0.5\,\mathrm{L\,min^{-1}}$ or less) via a manual needle valve. The "bypass" line carried the excess flow (approximately $8.5\,\mathrm{L\,min^{-1}}$), ensuring that the flushing of the inlet was maintained. Flow rates through the "sample" and "bypass" lines were monitored using $1\,\mathrm{L\,min^{-1}}$ and $30\,\mathrm{L\,min^{-1}}$ mass flow meters (TopTrak 822, Sierra Instruments Inc.; Figure 3, E and F), respectively. These flow meters recorded onto an SD card via microcontroller (Mega, Arduino; Figure 3, K), which in turn allowed for remote monitoring of the flow rates via the external USB bulkhead (Figure 1, D). Splitting the lines in such a way allowed the inlet pump to provide flow through both the Cold Trap collection vial and the inlet tubing.

3 Performance test data sets

3.1 Campaign site and weather conditions

The performance of the ICE-CUBE system was evaluated based on a field campaign data set obtained in challenging Arctic measurement conditions at the scientific settlement of Ny-Ålesund, Svalbard (Figure S2, Supplemental Material), during the ISLAS2020 campaign. The principal aim of the ISLAS2020 field experiment was to obtain detailed in-situ measurements of isotope fractionation in a Arctic environment, characterized by open fjord water and snow surface. Ny-Ålesund, with the adjacent strong air-sea interaction in the Fram Strait, is a well-suited location to make such observations. In particular during winter and spring, this region is frequently subject to periods of strong marine cold-air outbreaks, associated with intense evaporation (Papritz and Spengler, 2017).

In Ny-Ålesund, we deployed at two measurement sites, the first being approximately $300\,\mathrm{m}$ south of Ny-Ålesund, on the tundra (78.921 17 °N,11.913 61 °E). This site was also referred to as the "Snow" location and was used from 25–28 Feb 2020. The second site was located on a concrete pier at the northernmost edge of the settlement (referred to as "Fjord"; 78.928 73 °N,11.935 52 °E), and was used from 7–14 March 2020. The Profiling module utilized the tripod frame while at the Snow site, while it used the tipping frame at the Fjord site, to reach further down towards the surface of the water.

General $2\,\mathrm{m}$ air temperature and $10\,\mathrm{m}$ wind speed and gust information for the Ny-Ålesund weather station (SN99910) were retrieved from the Norsk Klimaservicesenter (https://seklima.met.no/observations). From this station dataset, $20\,\mathrm{year}$ climatological conditions were established by considering the hourly dataset of the period between 21 Feb and 14 Mar, between 2000 to 2019. The time period from 21 Feb to 14 Mar in Ny-Ålesund has a climatological median air temperature for 2000–2019 of $-12\,°\mathrm{C}$, with $50\,\%$ of hourly average temperatures being between $-16\,°\mathrm{C}$ and $-6\,°\mathrm{C}$ (Figure 4, black). In comparison, the majority of the ISLAS2020 campaign was spent in temperatures spanning -26 to $-18\,°\mathrm{C}$, with a median value of $-20\,°\mathrm{C}$ (Figure 4, blue). The coldest temperatures experienced during the campaign ($-30\,°\mathrm{C}$) were comparable to the minimum temperature in the 2000–2019 climatology, $-32.5\,°\mathrm{C}$ (Figure 4, black dashed line). Additionally, Dahlke et al. (2022) have identified Feb and Mar 2020 as having some of the strongest marine cold-air outbreaks of the last 42 years. Overall, with several episodes of extreme cold, our deployment was a formidable testing ground for the system.

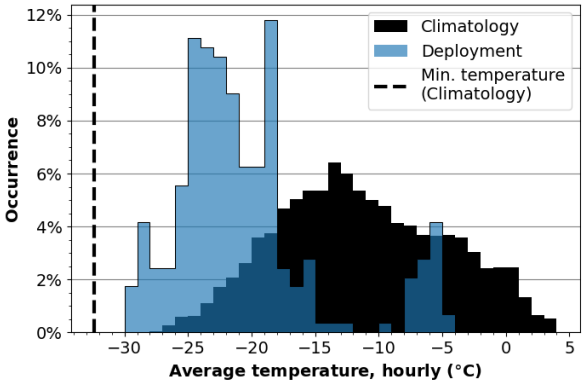

Figure 4. Histogram of hourly average temperatures in Ny-Ålesund for 2000–2019, 21 Feb to 14 Mar "Climatology" (black), alongside same from during the ISLAS2020 field campaign "Deployment" (blue). Black dashed line denotes minimum hourly temperature from the 2000–2019 period. Data from *Norsk Klimaservicesenter, Ny-Ålesund (SN99910)*.

3.2 Data processing

The ISE-CUBEs produce two main data streams, pertaining to the Analyzer, and Profiling modules, with each module internally recording its own respective stream. The Cold Trap expansion module does a similar task for its own data stream. An overview of the information contained in these data streams is given in Table 1. The isotopic data stream generated by the analyzer in the Analyzer module is the primary dataset, and also has the highest sampling frequency of $4\,\mathrm{Hz}$. The primary environmental parameters observed by the analyzer are humidity (volumetric mixing ratio), $\delta^{18}\mathrm{O}$, and $\delta\mathrm{D}$, alongside a multitude of analyzer diagnostic metrics, including temperatures and pressures internal components. Before further use, the isotope data set was calibrated and corrected as described in Sec. 3.3 below.

Both the Profiling and Cold Trap modules measure at $1\,\mathrm{Hz}$ via Arduino microprocessors, and record parameters to SD cards. The Profiling module records the temperature at the inlet head, in addition to height distances measured by the ultrasonic sensors. Laboratory calibration of the temperature probe showed a systematic offset of $0.67\,\mathrm{K}$, which is ac-

Table 1. Parameters logged by the ISE-CUBE system. '*' indicates parameters classified as metadata, providing information on the quality of the data collected. '**' While flow rates and metadata of Cold Trap module are recorded as 1 Hz, sample collection times varied.

Module	Parameter	Unit	Frequency
Analyzer	Isotopes (δ^{18}O, δD)	‰	4 Hz
	Humidity	ppm_v	4 Hz
	Analyzer diagnostics*		4 Hz
	(temperatures,	°C	4 Hz
	pressures,	Torr	4 Hz
	spectrographic fits)	-	4 Hz
Profiling	Inlet height	cm	1 Hz
	Inlet temperature	°C	1 Hz
Cold Trap	Flow rates	L/min	1 Hz
	Module temperature*	°C	1 Hz
	Cryocooler temp. range*	[FLAG]	1 Hz

counted for during post-processing. The Cold Trap expansion module monitors and records the flow through the collection vial, alongside remaining flow through the "bypass" line, as well as the temperature inside the module container. The same module also flags whether the cryogenic finger is within 5 K of the target temperature (−80 °C). Throughout the campaign, all module timestamps were compared to universal coordinated time, with offsets accounted for and datasets synchronised during processing.

The analysis of module performance that will follow in Sect. 4 makes use of datasets averaged across multiple time intervals. The technical analysis of Analyzer module performance in Sect. 4.1 and 4.2 uses a 1 s averaged dataset, as does the assessment of the Profiling module sensors in Sect. 4.3. However, subsequent evaluation of the Profiling module in regards to sample transmission uses the native 4 Hz resolution. Based on our system characterizations evaluated below, our final calibrated isotopic profiling dataset is averaged over 30 s (Sect. 4.4 and 4.5).

3.3 Isotope calibration and data processing

Requisite calibrations of the analyzer were performed immediately preceding and following deployment at each measurement site, at the Marine Laboratory in Ny-Ålesund. Isotopic measurements are calibrated on the VSMOW2-SLAP2 (Vienna Mean Ocean Water 2 - Standard Light Antarctic Precipitation 2) scale, composed of international, primary standards. The use of the scale allows for the relative ratios of heavy to light isotopes (R_{sample}) measured in CRDS analyzers to be normalized to a standard ($R_{standard}$), as described in Eq. 1 (Craig, 1961).

$$\delta^i = \left(\frac{R^i_{sample}}{R^i_{standard}} - 1 \right) \cdot 1000 \qquad (‰) \tag{1}$$

The value of the resulting δ^i (with i representing one of the heavy SWIs) is expressed in permil (per thousand, ‰). For our calibrations, we employed two secondary standards, whose isotopic values on the VSMOW2-SLAP2 scale have been established in the laboratory. The two secondary standards used were, DI (δ^{18}O=-7.68 ± 0.07 ‰ and δD=-49.7 ± 0.4 ‰) and GSM1 (δ^{18}O=-32.90 ± 0.05 ‰ and δD=-261.6 ± 0.3 ‰). Liquid standards were delivered with the Standard Delivery Module (SDM) device (A0101, Picarro Inc.), utilizing a Drierite filled moisture trap as a source of dry air. Only sufficiently stable calibration signals lasting longer than 10 minutes are considered for use in calibrating the dataset. As the specific humidity at the deployment site can be well below 3.5 g/kg for the time of year, a correction of the isotope composition was applied during post-processing, according to the quantified mixing ratio – isotope ratio dependency by Weng et al. (2020), specific to the analyzer used in the field. Several calibrations made during the ISLAS2020 field deployment were between mixing ratios of 3.5 g/kg and 0.5 g/kg, and confirm overall agreement with the mixing ratio – isotope ratio dependency determined in the laboratory.

Calibrations performed in the Marine Laboratory were considered valid only if they passed automatic quality control thresholds, such as humidity variation below 0.3 g/kg (500 ppmv). Across 17 valid calibrations, DI measurements had a standard deviation of 0.15 ‰ for δ^{18}O, and 0.48 ‰ for δD. For both isotope species, this standard deviation is similar (or smaller) than the standard deviation typical during any individual calibration. Total measurement drift across the campaign duration for DI was found to be smaller than these standard deviations. The GSM1 standard experienced technical issues with the SDM during multiple calibrations. The standard deviation across the 17 valid calibrations for this standard was 0.18 ‰ (δ^{18}O) and 0.47 ‰ (δD), again of a similar magnitude to the variabilities seen in individual calibrations. As for DI, the total measurement drift across the campaign duration for GSM1 was found to be similar to or smaller than these standard deviations. Overall, these drift values are compatible with the behavior exhibited by the same analyzer during previous use in the lab and field (Weng et al., 2020; Chazette et al., 2021) and exceed the manufacturers typical performance specifications (Picarro Inc., 2021).

3.4 Analyzer performance benchmark periods

We introduce two reference periods for comparison to our analyzer's behavior in the field. The first represents the optimal operating environment for the analyzer, a well-controlled laboratory setting with ambient room temperatures of approximately 20 °C. This first period runs from June–July 2020 when the same analyzer was used at FARLAB, University of Bergen, Norway. During this time, the analyzer was routinely sampling standard vapor with mixing ratios down to 0.155 g/kg, comparable to humidity minimums en-

countered in the field. The second period, more closely resembles a typical deployment, with the instrument sampling exterior air through an inlet tube while installed inside a building with a controlled environment, but less stringently regulated than a university research laboratory. During this short-term deployment, the same analyzer was installed at the Zeppelin mountain observatory ($475\,\mathrm{masl}$), $2\,\mathrm{km}$ SSW of Ny-Ålesund. The installation spanned from 29 Feb 2020 to 2 Mar 2020, with the analyzer measuring outside the ISE-CUBE module. Both reference periods sampled at $1\,\mathrm{Hz}$, and at a lower flow rate than we used in the field. Across the three environments, we compare the overall analyzer temperature, the cavity temperature and pressure, and the temperature of the "warm box", an enclosure housing essential analyzer electronics critical for spectroscopic fitting.

3.5 Additional datasets

Since 2010 the Alfred Wegner Institute (AWI) has operated the Ny-Ålesund eddy-covariance (EC) site (Jocher et al., 2012; Schulz, 2017), about $300\,\mathrm{m}$ south of the settlement and approximately $20\,\mathrm{m}$ away from the ISE-CUBE system during the initial deployment phase at Snow. This EC station measures, amongst others, air temperature at $1.0\,\mathrm{m}$, averaged over $30\,\mathrm{s}$. Temperatures are measured at by a Thies Clima compact temperature sensor (2.1280.00.160, Adolf Thies GmbH & Co. KG, Germany), inside a ventilated shield (1.1025.55.100, Adolf Thies GmbH & Co. KG, Germany). This temperature was used for field validation of the temperature probe fixed to the head of the Profiling module, as described in Appendix C.

4 Results

We now detail how the field conditions influenced analyzer performance and thus data quality, using the laboratory and observatory periods as performance benchmarks. Thereby, we focus first on temperature and pressure conditions of the analyzer (Sect. 4.1), before evaluating the impact of field conditions on the water isotope measurements (Sect. 4.2). Then we detail the performance of the profiling module, especially the capability of the module to deliver sample to the analyzer for the purpose of resolving vertical profiles (Sect. 4.3). Finally, the performance of the cold trap expansion module is briefly presented (Sect. 4.4).

4.1 CRDS analyzer response to ambient conditions

Using our laboratory and observatory benchmarks, we now detail how the field conditions influenced analyzer performance and thus data quality. We first use the Data Aquistion System (DAS) temperature (T_{DAS}) measured inside the analyzer housing as a proxy of the overall temperature and condition of the analyzer (Picarro Inc., 2013). Then, we characterize the measurement cavity through its temperature (T_{C}) and pressure (p_{C}). Finally, we study essential analyzer electronics, namely the Wavelength Monitor (WLM), via the warm box temperature (T_{WB}).

4.1.1 Overall analyzer temperature

The T_{DAS} serves as a first-order proxy for the overall measurement environment of the analyzer. As the T_{DAS} results from a balance between radiant, excess heat from other components (especially from the measurement cavity) and constant ventilation with ambient air, its value can span a wide range. In the laboratory, T_{DAS} values are typically within a narrow distribution, with $94.3\,\%$ of T_{DAS} falling within 45 to $50\,^{\circ}\mathrm{C}$ (Figure 5a, black). This narrow distribution is similar for the observatory ($91.7\,\%$ within 47.5 to $52.5\,^{\circ}\mathrm{C}$). In contrast, the most frequent T_{DAS} from the field is within the 30 to $32.5\,^{\circ}\mathrm{C}$ range ($17.3\,\%$) (Figure 5a, blue bars). Across all percentiles (Table 2), the T_{DAS} in the field is lower and more broadly distributed. Thus, the overall temperature of the analyzer was colder and more variable in the field as compared to the lab. However, the T_{DAS} stayed within its necessary range for operation, with the analyzer remaining functional for the entirety of the two deployments. Therefore, any further impacts from this increased variability require exploration. We now continue our investigation with the conditions in the measurement cavity, the most critical element of the analyzer.

4.1.2 Cavity temperature and pressure

The precision and accuracy of the temperature inside the measurement cavity of the analyzer is of the utmost importance for precise spectroscopic measurements. For this reason, the analyzer regulates the cavity temperature very precisely about $80.00 \pm 0.01\,^{\circ}\mathrm{C}$ (Steig et al., 2014). The median T_{C} is identical across the field, laboratory, and observatory periods, $80.000\,^{\circ}\mathrm{C}$ (Figure 5b and Table 2). Between the 95^{th} and 5^{th} percentiles, T_{C} distributions between field and laboratory are indistinguishable from one another. In the field, the cavity temperature stays within this range for $99.99\,\%$ of the time, which exceeds the laboratory benchmark ($99.97\,\%$). Finally, there exists no correlation between T_{C} and T_{DAS} while deployed in the field. Therefore, $99.99\,\%$ of field observations are made with cavity temperatures within specified limits, and are indistinguishable from the laboratory benchmark.

The pressure inside the cavity must be maintained at $66.66 \pm 0.10\,\mathrm{hPa}$ (Steig et al., 2014). The ISE-CUBE system does little to modify the native flow pattern of the analyzer, therefore we expect that the p_{C} exhibits no dependence on the DAS temperature. Just as with T_{C}, there is no correlation between p_{C} and T_{DAS} while deployed in the field. Overall, the specified range is maintained for $99.95\,\%$ of the field deployment, which differs from our laboratory benchmark ($99.99\,\%$). Indeed, both the laboratory and observatory reference periods have slightly narrower distributions (Figure 5c

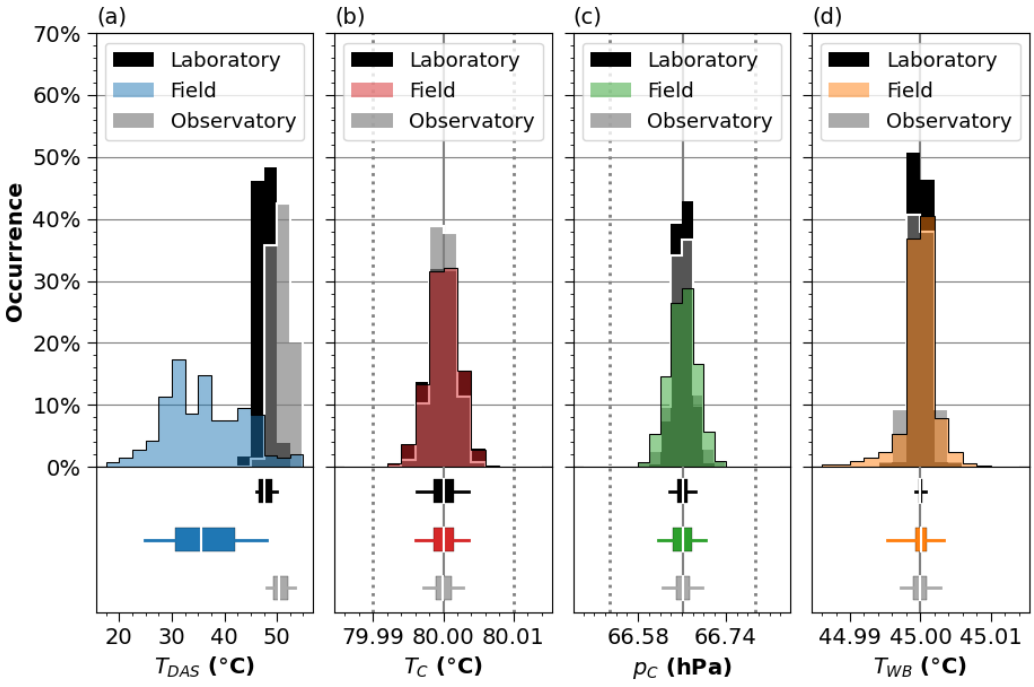

Figure 5. Relative occurrence of (a) DAS temperatures, T_{DAS} (2.5 °C bins), (b) Cavity temperatures, T_{C} (0.002 °C bins), (c) Cavity pressures, p_{C} (0.02 hPa bins), and (d) Warm Box temperatures, T_{WB} (0.002 °C bins) during CRDS operation, for field deployment periods (colored) as compared to reference periods, laboratory (black) and observatory (gray). Lower panels show total distributions for the three periods in boxplot form, with the median (white line), Interquartile Range (IQR) (box limits), and 95$^{\mathrm{th}}$ and 5$^{\mathrm{th}}$ percentiles (whiskers). Solid vertical lines for b), c), and d) indicate parameter target value. Dotted lines for b) and c) indicate instrument control precision as per manufacturer. Note that "Field" and "Laboratory" overlap closely in b).

Table 2. Analyzer statistics for the overall analyzer temperature (T_{DAS}), the cavity temperature and pressure (T_{C} and p_{C}), and the warm box temperature (T_{WB}). Percentile intervals as indicated from field, laboratory, and observatory periods. Corresponding 95$^{\mathrm{th}}$ to 5$^{\mathrm{th}}$ span provided for the same.

		Percentile					
	Location	5th	25th	50th	75th	95th	95th-5th
T_{DAS} (°C)	Lab	46.1	46.6	47.6	49	49.9	3.8
	Obs	48.0	49.2	50.3	52.2	53.4	5.4
	Field	24.8	30.8	35.6	42.1	48.0	23.2
T_{C} (°C)	Lab	79.996	79.999	80.000	80.001	80.004	0.008
	Obs	79.997	79.999	80.000	80.001	80.003	0.006
	Field	79.996	79.999	80.000	80.001	80.004	0.008
p_{C} (hPa)	Lab	66.64	66.65	66.66	66.67	66.69	0.05
	Obs	66.63	66.65	66.66	66.67	66.70	0.07
	Field	66.62	66.64	66.66	66.68	66.70	0.08
T_{WB} (°C)	Lab	44.999	45.000	45.000	45.000	45.001	0.002
	Obs	44.997	44.999	45.000	45.001	45.003	0.006
	Field	44.995	44.999	45.000	45.001	45.003	0.008

and Table 2). So even though the cavity pressure remained within limits for the vast majority of the time, some aspect of the field deployment had an impact on cavity variability. After further investigation into other potential differences between the laboratory and field setups, we determined that this difference in cavity pressure variability stems from the enhanced sample flow configuration of the analyzer while being used in the field (Sect. 2.2), and is not inherent to a specific aspect of the ISE-CUBE system. The fast-response configuration on this instrument has been used in a previous field deployment (Chazette et al., 2021), and is within the scope of the standard operating procedures.

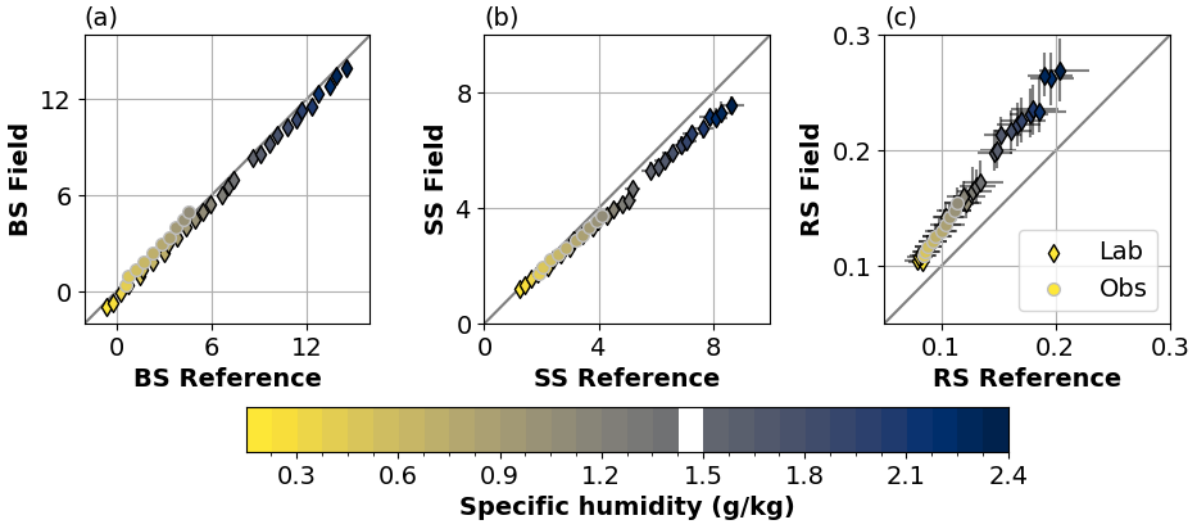

Figure 6. (a) Baseline Shift, (b) Slope Shift, and (c) Residuals of the expected model spectrum versus the fitted absorption spectrum from the analyzer's WLM, for field periods where the warm box temperature is above the 95th or below the 5th percentiles. Light gray line represents 1-to-1 ratio. Data are divided into $0.075\,\mathrm{g/kg}$ bins, from 0.15 to $2.4\,\mathrm{g/kg}$ (colorbar), with error bars denoting IQR for both field and reference measurements.

In summary, the accuracy and precision of cavity pressure and temperature remained within necessary limits, and were comparable to our two benchmark periods. In particular, the cavity temperatures were indistinguishable between laboratory and field. We therefore expect the measurement cavity to have been functioning reliably during the field deployment. As a final analyzer parameter, we now investigate the warm box temperature.

4.1.3 Warm Box temperature

The WLM is part of the analyzer's laser control loop and is continuously used to target the desired wavelengths, reducing instrument drift (Crosson, 2008; Gupta et al., 2009). It is contained within the Warm Box, which the analyzer regulates the interior temperature to $45\,^{\circ}\mathrm{C}$. In our laboratory benchmark, $90\,\%$ of the variation about this target was within $0.002\,^{\circ}\mathrm{C}$ (Table 2). In comparison, the same range of T_{WB} in the field, has four times the variability (Table 2). The field distribution is more similar to our observatory benchmark period (Figure 5d and Table 2). Even when compared to this benchmark, T_{WB} from the field has a tendency towards lower temperatures (Figure 5d). This indicates that the temperature inside the Warm Box is coupled to the changing (usually cooling) analyzer temperature. Since the analyzer has a gas inlet at the back, leading to the WLM, ambient air temperature could also more directly impact the T_{WB} than other components. As an example, sudden dips and spikes in T_{WB} correspond with the onset of drops and rises in T_{DAS} (Figure S3, Supplemental Material). As this range of variations could potentially have an impact on measurement quality, we now assess WLM performance in more detail during lab and benchmark.

For the evaluation of the WLM performance, we use three spectroscopy metrics that quantify the difference between an expected model spectrum versus the fitted absorption spectrum that is actually measured by the analyzer (Johnson and Rella, 2017). The baseline shift (BS) describes the absolute value change of the spectral baseline, the slope shift (SS) indicates the change in the slope of the baseline (Johnson and Rella, 2017; Weng et al., 2020), and the residual (RS) represent the residual errors present in the fit spectrum, compared to the expected spectrum. The spectra have a first-order dependency on mixing ratio with resulting baseline differences (Aemisegger et al., 2012; Steen-Larsen et al., 2013, 2014; Bonne et al., 2014; Weng et al., 2020). To account for this dependency on the isotopic concentrations derived from the spectra, data from both field and reference periods have been sorted into $0.075\,\mathrm{g/kg}$ bins, from 0.150 to $2.400\,\mathrm{g/kg}$. For field measurements, only instances when the T_{WB} is above the 95th or below the 5th percentiles are considered. In our laboratory benchmark, only periods using synthetic air ($80\,\%$ N_2, $20\,\%$ O_2) as a carrier gas are considered. Specifically, these periods consist of seven multi-point humidity calibrations (Figure B1, d-j) with a lab standard being of a similar depletion (δ^{18}O: $-40.02 \pm 0.07\,‰$ and δD: $-307.8 \pm 0.8\,‰$) as the field.

Figure 6 displays a comparison between the three metrics during reference periods against field operation. Ideal analyzer performance would produce a strong correlation in the three metrics between field and reference data, while also

aligning closely to a 1-to-1 line. All three metrics have correlations above 0.990, for both laboratory and observatory (Table 3). Additionally, our two reference periods have comparable values, at similar specific humidity concentrations (Figure 6). The BS and SS also have linear regression line slopes near to 1. The RS error has the linear regression with the largest deviation from 1, (1.35 ± 0.03 and 1.49 ± 0.11, for laboratory and observatory, respectively) with an intercept within 0.02 (Table 3). While analyzer performance to first order appears as desired, this consistently larger RS error of the field indicates that the spectral fit in the field was not as good as in the reference periods. The fits are also similar when all T_{WB} values are considered and not only above the 95$^{\mathrm{th}}$ or below the 5$^{\mathrm{th}}$ percentiles. While this indicates that the measurements in the field have the potential for larger uncertainty, obtaining an exact quantification of uncertainty from this difference is non-trivial and requires access to proprietary analyzer details. Therefore, we now proceed with an alternative method to quantify the quality of the water isotope measurements from the ISE-CUBE system.

Table 3. Correlations and linear regression values (slope and intercept) for WLM metrics (Baseline shift, BS; Slope shift, SS; and Residuals, RS) in field vs. reference period.

		Field vs. Laboratory	Field vs. Observatory
BS	Correlation	0.999	0.995
	Slope	0.99 ± 0.01	1.07 ± 0.06
	Intercept	-0.42 ± 0.07	-0.03 ± 0.18
SS	Correlation	0.998	0.995
	Slope	0.88 ± 0.02	0.86 ± 0.05
	Intercept	0.08 ± 0.08	0.16 ± 0.16
RS	Correlation	0.991	0.991
	Slope	1.34 ± 0.05	1.49 ± 0.11
	Intercept	0.00 ± 0.01	-0.02 ± 0.01

4.2 Measurement quality of water vapor isotopes

Based on the assessment of analyzer parameters presented above, measurement conditions within the ISE-CUBE system and in the laboratory differ mostly with respect to the variability of T_{WB} and T_{DAS}. To identify a potential impact of this temperature variability on the vapor isotope measurements, we now compare the variability of the isotopic signal between our reference periods and the field. Since mixing ratio (and thus the amount of molecules in the measurement cavity) is a key factor in the precision of the CRDS measurements, we divide the measurement data into 15 bins from 0.150 to $2.400\,\mathrm{g/kg}$, $0.150\,\mathrm{g/kg}$ wide; similar to the bins as we used before in Sect. 4.1.3, though twice as wide.

For our field period, we first partition our measured humidities by site; in this way, we ensure that measurement conditions at each site are represented. Then, we identify the distribution of measured humidities at each site according to our bins, and normalize it to 100 for the Snow site and 200 for the Fjord site. Then, occurrence in each bin is rounded up to the nearest whole number, such that the smallest bin contains at least two points. Finally, for each site and bin, we identify a corresponding number of $5\,\mathrm{minute}$ windows with the most stable mixing ratios (i.e. lowest standard deviation of humidity), as categorized by the mean across the $5\,\mathrm{minutes}$. The maximum standard deviation across all $5\,\mathrm{minute}$ windows in the field was $0.030\,\mathrm{g/kg}$, with the median being $0.002\,\mathrm{g/kg}$. A similar procedure was done for the observatory reference period, though standard deviations were lower than in the field. Within the laboratory benchmark, we focus on ten distinct usage events conducted for instrument characterization purposes (Figure B1). During these events, the analyzer was subjected to step-wise mixing ratio sequences between 0.20 and $2.25\,\mathrm{g/kg}$ (Figure B1). The steps usually lasted 5 to $10\,\mathrm{minutes}$, and the sequences did not necessary follow a consistent step magnitude. Similarly as to the field and observatory, the most stable $5\,\mathrm{minute}$ window were identified, using a cut-off threshold of $0.006\,\mathrm{g/kg}$. These sequences used a standard of a similar depletion (δ^{18}O: $-40.02 \pm 0.07\,‰$ and δD: $-307.8 \pm 0.8\,‰$) as our field measurements. For laboratory, observatory, and field, the 1-σ $5\,\mathrm{minute}$ standard deviation over each of these windows was then calculated for both δ^{18}O and δD.

For all three periods, and for both δ^{18}O and δD, the measurement precision decreases with decreasing mixing ratio (Figure 7a,c). The same is true of the d-excess (Figure 7e). In the lowermost bin of 0.150 to $0.300\,\mathrm{g/kg}$, $5\,\mathrm{minute}$ standard deviations in the field reach up to $1.0\,‰$ for δ^{18}O (Figure 7a), and $8\,‰$ for δD and the d-excess (Figure 7c,e), whereas the same in the laboratory reference are around $0.7\,‰$ (δ^{18}O) and $5\,‰$ (δD and d-excess). Across all humidities, field bin means (thick colored line) are consistently higher than laboratory and observatory bin means (Figure 7a,c,e; black and gray/white lines, respectively). This difference between field and reference periods (Figure 7b,d,f) increases at lower humidities, and is consistent between reference periods. A logarithmic fit (Figure 7b,d,f; thick colored lines) gives the maximum increase in measurement uncertainty (at the minimum humidity value from the field, $0.197\,\mathrm{g/kg}$) as $0.15\,‰$ for δ^{18}O, $1.35\,‰$ for δD, and $1.42\,‰$ for d-excess. According to this fit, the median humidity value from the field ($0.562\,\mathrm{g/kg}$) would have associated increases of uncertainty in δ^{18}O, δD, and d-excess of $0.10\,‰$, $0.89\,‰$, and $0.93\,‰$, respectively. Averaged across humidity bins, this corresponds to a variability increase of $30\,\%$ in the field compared to the laboratory benchmark, though the largest relative increase occurs at the higher humidities.

In summary, the field deployment exhibits consistently higher variability for isotopic measurements, as compared to the optimal measurement conditions in a well-controlled research laboratory. This higher variability in the field is likely

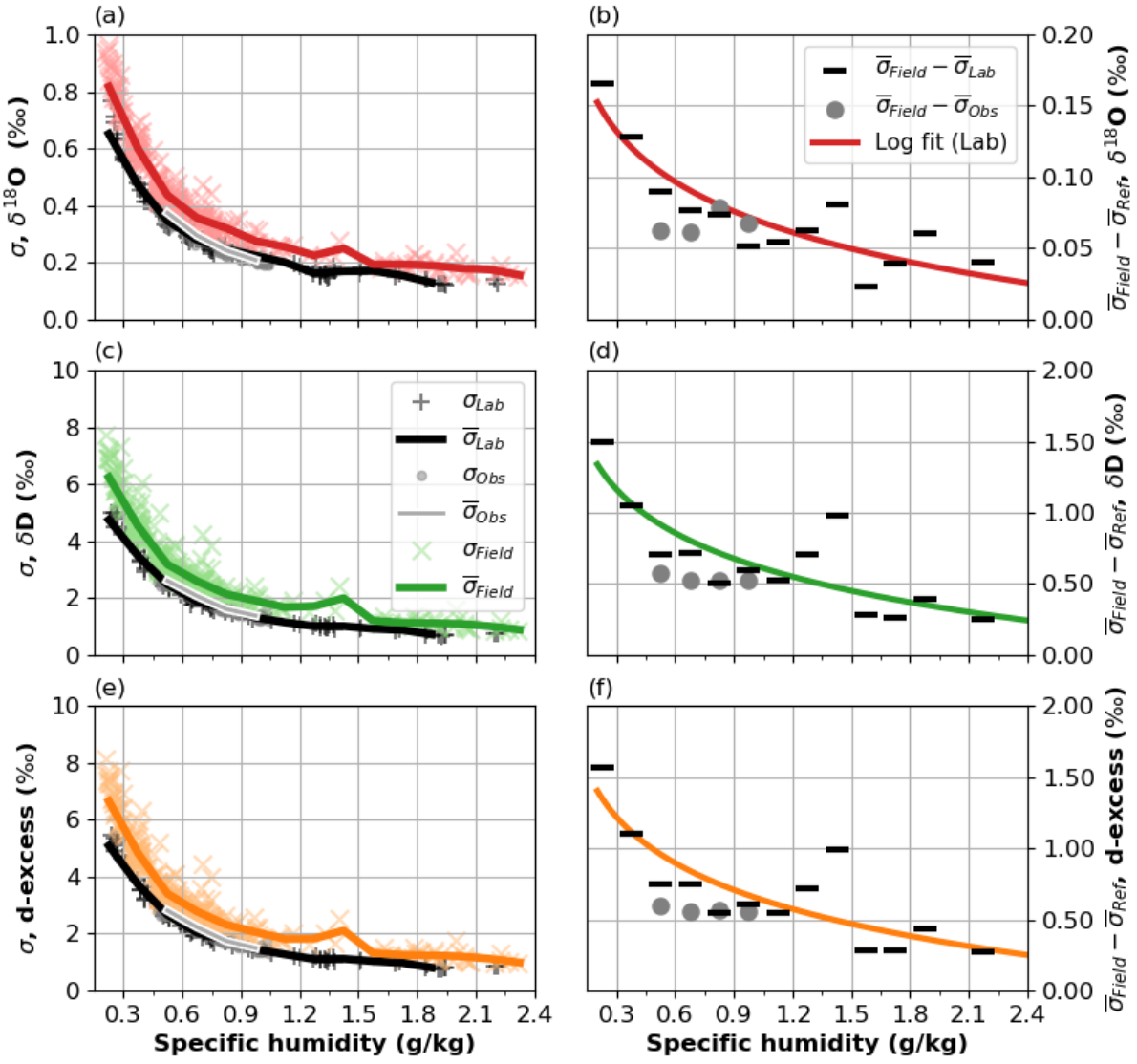

Figure 7. Standard deviations of δ^{18}O, δD, and d-excess in field and reference periods, alongside differences between periods. Measurements organized across $0.15\,\mathrm{g/kg}$ bins, from 0.15 to $2.40\,\mathrm{g/kg}$. (a) Standard deviations of δ^{18}O over $5\,\mathrm{min}$ periods from field (colored 'x'), laboratory (black '+', and observatory (gray 'o')); see text for details. Bin means depicted with thick lines. (b) Differences between bins means from field and laboratory (black ticks) and field and observatory (gray circles) periods. Thick colored line indicates the logarithmic fit of field-lab differences. (c,d) Same as (a,b) but for δD. (e,f) Same as (a,b) but for d-excess.

a consequence of the more variable T_{WB} and T_{DAS}, but could also be due to the more variable composition of the ambient air used to quantify stability. Additionally, we have not investigated the contribution that our increased flow configuration (Sect. 2.2) might have on this increase in variability. Therefore, we proceed under the premise that our obtained measurements have an increased uncertainty associated with the conditions and the deployment system, as described by the calculated logarithmic fits. Nonetheless, we will show that though this decreased precision is inherent to the observations, it does not hinder useful measurements, in particular since the measurement precision is quantified.

4.3 Profiling module performance

Evaluation of the Profiling module is divided into sensor performance and sample transmission. Sensor performance details of the ultrasonic distance sensor and the temperature probe at the tip of the inlet are found in Appendix C. We now

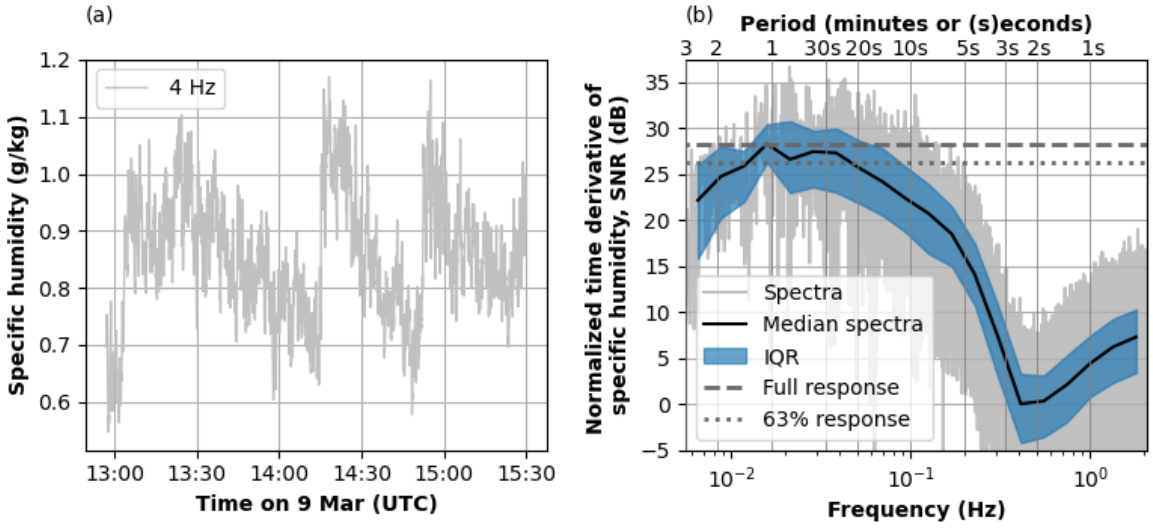

Figure 8. Inlet response determination for the profiling period on 9 Mar 2020, from 12:57 to 15:30 UTC. (a) The 4 Hz specific humidity signal as measured by the analyzer. (b) The fast Fourier transform of the normalized time derivative of the specific humidity (gray), expressed as a signal to noise ratio. Black line is the median of the resulting power spectra, across 20 logarithmically spaced bins between between 5.55×10^{-3} and 2 Hz, while colored shading is the interquartile range (IQR) of the bin. The minimum of the median (at approximately 0.4 Hz or 2.5 s) serves as noise baseline, where as the maximum signifies the full response (dashed gray line). Dotted line indicates 63 % of the full response.

assess the Profiling module's ability to transmit sample to the analyzer, including its capacity to resolve isotopic profiles.

The time it takes for the analyzer to react to a step change in humidity at the inlet head is predominantly governed by the length of the inlet tubing and the flow rate through it. With the heated tubing from inlet tip to the sample port of the analyzer having a diameter of 4.5 mm, and at a flow rate of about 9 L min^{-1} in the Profiling module tubing, and 0.15 L min^{-1} in the inlet assembly, the minimum response time would be approximately 6 s. We were unable to conduct any controlled single-step changes during the field deployment, as we lacked a suitable field device to produce a defined vapor isotope stream at sufficiently high flow rates. However, profiling with the articulating arm approximated multiple step changes, albeit without a controlled humidity source. We take the profiling period from the Fjord site on 9 Mar 2020, which included multiple abrupt humidity changes as we stepped through profiling levels, with some step changes reaching 0.3 g/kg (Figure 8a). Therefore, we followed the approach of Steen-Larsen et al. (2014) and Wahl et al. (2021), and applied a fast Fourier transform analysis to the normalized time derivative of the specific humidity observed during this profiling period (Figure 8b). We then consider the median across 20 logarithmically spaced bins, between 5.55×10^{-3} and 2 Hz, of the resulting power spectra as a signal to noise ratio (SNR) (Figure 8b, blue line), with the spectral minimum defining our baseline at approximately 0.4 Hz or 2.5 s. We see that the signal reaches 63 % of its full response after approximately 20 s, however, by 30 s the signal is 80 % of full response. These statistics are also similar, though less strong, for the low humidities encountered at the Snow site (Figure S4, Supplemental Material). Therefore, we conclude that the system is capable of producing a dataset with 30 s resolution, which can be used for analysis purposes.

Next, we consider the minimum duration required at a particular height to resolve the isotopic profile. We again take our profiling period on 9 Mar 2020, now examining the isotopic measurements (Figure 9a,c,e). We apply a fast Fourier transform on the 4 Hz isotopic signal to obtain a power spectrum across a range of frequencies/periodicities (Figure 9b,d,f). The spectra median (across 20 logarithmically spaced bins between 8.33×10^{-4} and 2 Hz) (Figure 8b,d,f; thick black lines) indicate a baseline extending from 2 Hz until approximately 0.1 Hz (10 s). Frequencies higher (periodicities smaller) than this are considered to be indistinguishable from noise. The 25$^{\text{th}}$, and especially the 75$^{\text{th}}$ percentiles for these frequencies are also mostly constant (Figure 9b,d,f; colored shading). At periods larger than 20 s, the signal begins to emerge from the noise. The d-excess signal takes the longest to emerge, with the median SNR surpassing the 75$^{\text{th}}$ percentile of the noise level (Figure 9f; dotted line) at 1.5 minutes. This means that 50 % of the frequencies at this point have a higher SNR than 75 % of the noise. Periodicities smaller than this have less than twice as much power as the noise median, and cannot be resolved. After 2 minutes, the median signal reaches 5 dB, or approximately 3.16 times the median noise baseline; periodicities larger than this can begin to be resolved. At periodicities of 4 minutes, medians of all isotopic signals have an SNR larger or equal to 10 dB.

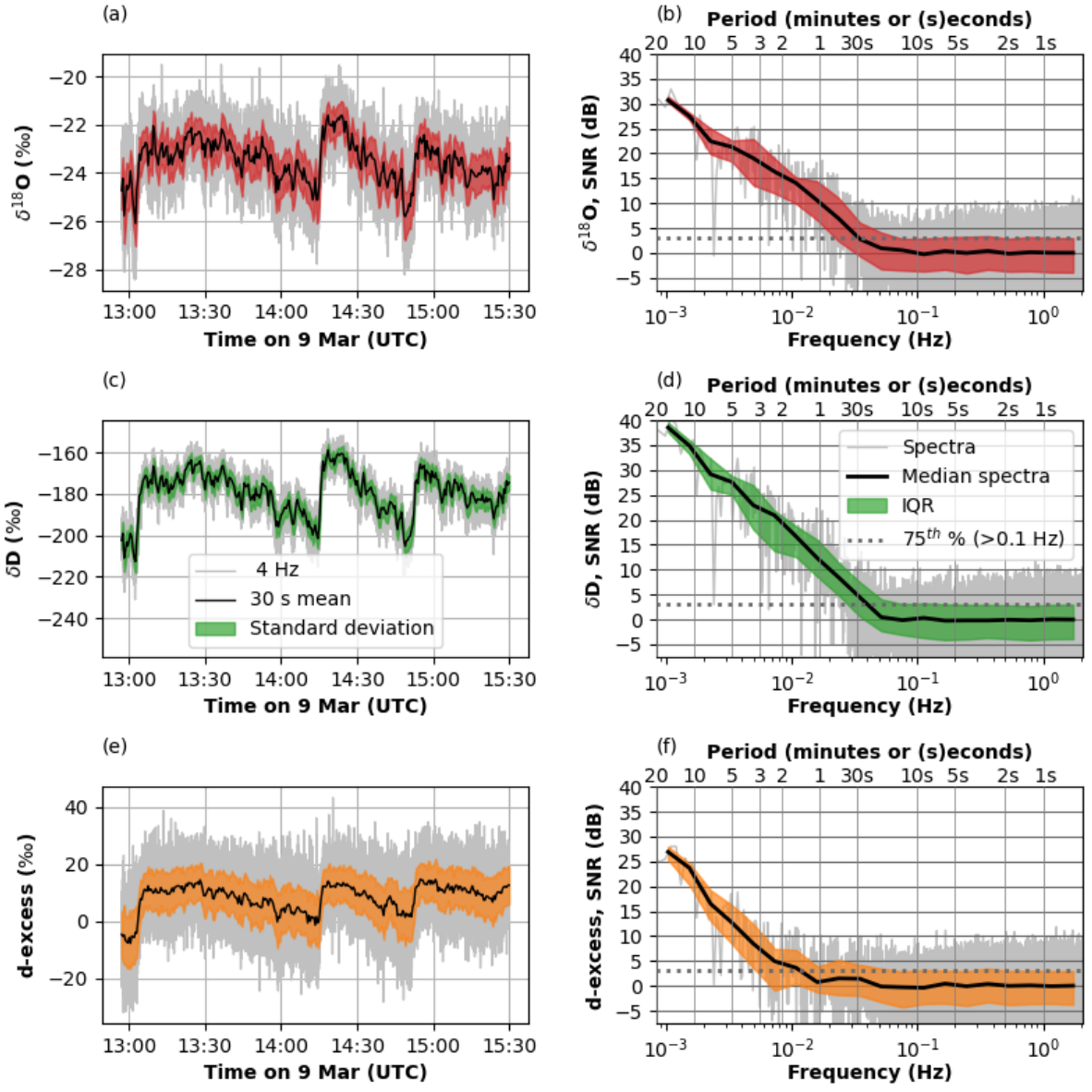

Figure 9. Resolving isotopic signals during the profiling period on 9 Mar 2020, from 12:57 to 15:30 UTC. (a) The 4 Hz δ^{18}O signal (gray), with the 30 s mean (thick black) and standard deviation of the same (colored shading). (b) The fast Fourier transform of δ^{18}O (gray), expressed as a signal to noise ratio. Black line is the median of the resulting power spectra, across 20 logarithmically spaced bins between between 8.33×10^{-4} and 2 Hz, while colored shading is the interquartile range (IQR) of the bin. Dotted line is the mean of the 75$^{\text{th}}$ percentile for frequencies larger than 0.1 Hz. (c,d) Same as a,b), but for δD. (e,f) Same as a,b), but for d-excess.

At the less humid Snow site, the median SNR is equal to or above 5 dB after 4 minutes (Figure S5, Supplemental Material). Therefore, across both deployment sites, we determine that maintaining a single height for at least 4 minutes is necessary to begin to resolve the signal during profiling, though longer durations will yield a higher resolving power.

4.4 Cold Trap module performance

The Cold Trap expansion module was fully integrated into the sample air flow of the ISE-CUBE system during the field tests. Since the Cold Trap box was not thermally regulated, the cryocooler unit was operated well below the manufacturers minimum operating guideline of 5 °C, reaching −5 °C over sustained periods, and even down to −20 °C occasionally. Nonetheless, the cryocooler reliably provided tempera-

Table 4. δ^{18}O and δD measurements for two time periods as observed by the CRDS analyzer (Integrated vapor) and as collected by the Cold Trap (Collected sample), alongside the differences between.

Time span	Isotope	Integrated vapor (‰)	Collected sample (‰)	Difference (‰)
2020-02-25 15:20:00 to	δ^{18}O	-34.07 ± 0.87	-33.89 ± 0.08	0.18 ± 0.87
2020-02-26 08:50:00	δD	-274.6 ± 1.2	-244.5 ± 0.4	30.1 ± 1.3
2020-03-08 17:25:00 to	δ^{18}O	-27.10 ± 0.87	-25.90 ± 0.07	1.20 ± 0.87
2020-03-09 08:20:00	δD	-220.0 ± 1.2	-193.7 ± 0.4	26.3 ± 1.3

tures of $-80 \pm 5\,°\mathrm{C}$ at the base of the vial enclosure for $80\,\%$ of the deployment. The remaining $20\,\%$ mostly occurred during overnight collections, whereby excessive frost buildup on the exterior of the brass vial enclosure would provide additional insulation and the vial temperature would drop below $-85\,°\mathrm{C}$. Vapor collection in a vial lasted between $8\,\mathrm{hours}$ and $16\,\mathrm{hours}$ during daytime and nighttime, with target flow rates of $0.5\,\mathrm{L\,min^{-1}}$ and $0.25\,\mathrm{L\,min^{-1}}$, respectively. Water vapor was successfully collected during a total of 28 periods, with up to $0.3\,\mathrm{mL}$ in a single sample, though some samples collected significantly less.

We now present a comparison between two collected samples and the mass-flow integrated isotope measurements from the analyzer for the same period (Table 4). One sample is from during the Snow deployment, while the other is from the time at the Fjord. While δ^{18}O values are close to being within measurement error, the δD values are quite different. This is likely due to a combination of deficiencies involving sample collection, inconsistent flow regulation, and possibly fractionation effects at the low temperatures in the glass sample vial. These fractionation effects might arise from incomplete freeze out of the vapor, induced by insufficient thermal stability of the glass collection vial. We additionally observed substantial ice crystal formation in the neck of the collection vials, which inhibited and decreased flow during multiple collection periods. This ice formation also compromised sample recovery during vial exchange, causing frozen sample to fall out of the vial during collection. Therefore, the disagreement between sample and analyzer measurements is not unexpected, especially as the collected sample would no longer correspond with the integrated time period being compared with.

In summary, we provide here a first proof-of-concept that a cryocooler-based Cold Trap module can be integrated into the ISE-CUBE system. The deficiencies identified could be corrected with a different collection vial and a better flow regulator (i.e. a mass flow controller), although sample analysis procedure would need to be changed. A more detailed evaluation of the performance of the Cold Trap module in terms of sampling efficiency and its suitability for in-field calibration is however beyond the scope of this manuscript and will be detailed in a future publication.

4.5 Example of a profiling operation

We now present an example for a profiling operation at the Fjord site on the afternoon of 9 Mar 2020, from 12:57 to 15:30 (UTC). Winds during this period were fairly constant around $7\,\mathrm{m\,s^{-1}}$, occasionally gusting to $9\,\mathrm{m\,s^{-1}}$. The entire profiling operation consisted of a sequence of 19 steps across three cycles, performed at heights between $1.5\,\mathrm{m}$ and $3.5\,\mathrm{m}$ above the surface of the water (Figure 10a, black line). Throughout the profiling operation, mean air temperature at the inlet and mean specific humidity were anti-correlated with height (Figure 10a, cyan and blue lines, respectively). The profiling head was kept at any particular height for 4.5 to $13\,\mathrm{minutes}$ (Figure 10a, yellow highlights), with the first $30\,\mathrm{s}$ at the level disregarded. For these periods, we calculated the corresponding means for the humidity, temperature, δ^{18}O, δD, and d-excess (Figure 10b-e, colored markers), alongside the standard errors of the means with a $99\,\%$ confidence interval (Figure 10b-e, black errorbars). We also calculated the observed variability (standard deviation) of the measured quantities (Figure 10b-e, gray errorbar), including the system uncertainty as calculated in Sect. 4.2 (Figure 10c-e, gray ticks on errorbar). We found the variability to be a similar magnitude for all height levels, regardless of sampling duration, with the system uncertainty accounting for approximately half the variability at any particular height.

Across the $2\,\mathrm{m}$ profile span, a linear fit through the mean humidities yielded a gradient (with 95% confidence interval) of $-0.13 \pm 0.04\,\mathrm{g/kg/m}$ (Figure 10b, blue). The linear fit for air temperature was $-0.63 \pm 0.17\,\mathrm{K/m}$ (Figure 10b, cyan). This was to be expected, as the surface of the water was a source of both heat and moisture. The isotopic signature of the moisture also exhibited a gradient. δ^{18}O, δD, and the d-excess (Figure 10c,d,e) all display negative gradients across their linear fits ($-0.86 \pm 0.49\,‰/\mathrm{m}$, $-13.4 \pm 5.3\,‰/\mathrm{m}$, and $-6.52 \pm 2.17\,‰/\mathrm{m}$, respectively). The profiles, especially those for δD and the d-excess, have a strong correlation with height, and the derived linear gradients have a narrow $95\,\%$ confidence interval (Figure 10b-e; black shading).

5 Discussion

With the ability to resolve near-surface profiles, the ISE-CUBE system offers a number of advantages over a valve/manifold combination. Fundamentally, the profiling

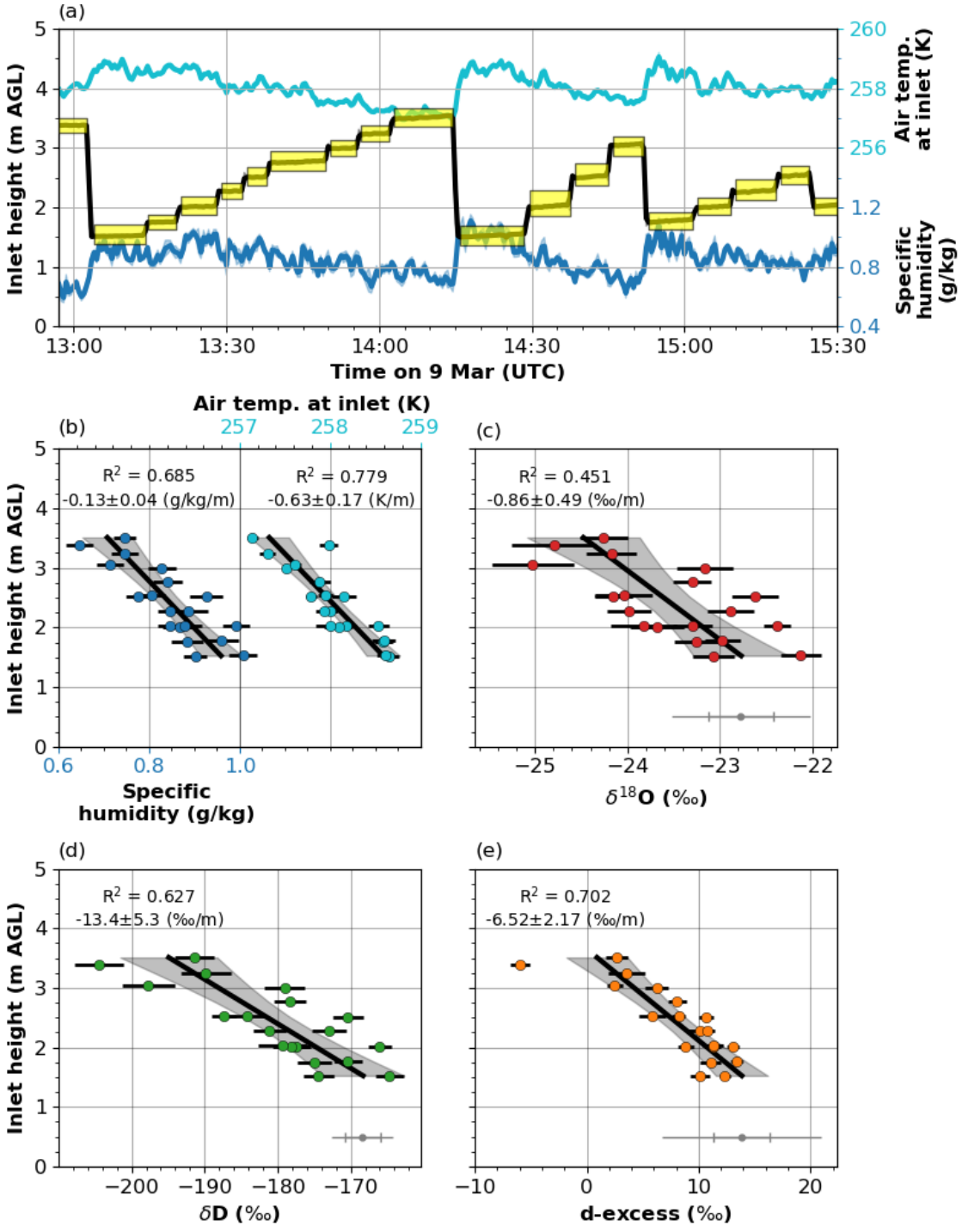

Figure 10. A profiling operation from 12:57 to 15:30 on 9 Mar 2020. (a) A time series of inlet head height (black lines, left axis), alongside the air temperature at the same (cyan line, upper right axis) and specific humidity (blue line, lower right axis). 19 height levels and their durations denoted with yellow highlighting. (b) Vertical profiles of the air temperature at the inlet head (cyan, upper-right axis) and specific humidity (blue, bottom-left axis). Errorbars signify standard errors, with 99 % confidence interval. Thick black line is the linear regression through the data points, with shading showing 95 % confidence interval. (c) Same as b), but for δ^{18}O. (d) Same as b), but for δD. (e) Same as b), but for d-excess. Lower gray marker and errorbar is a variability scale denoting a representative standard deviation for any particular height, with system uncertainty as calculated in Sect. 4.2 indicated as ticks.

arm allows for increased continuity in the observed profiles, as compared to a fixed height tower. The freedom to chose any height in the $2\,\mathrm{m}$ range enabled us to produce fine-scale vertical profiles with a resolution of approximately $25\,\mathrm{cm}$. Though this particular interval is arbitrary, being able to select heights of interest while measuring led to a more dynamic sampling strategy that could be adapted on-the-fly. Duplicating a profile such as obtained on 9 Mar would involve an approximate eightfold increase in the number of inlet lines, without any guarantee that an inlet would be at a height of interest. Unlike typical tower measurements, the short inlet lines of the Profiling module allow for rapid instrument response, and limit potential wall interactions with the tubing during sample transmission. These short inlet lines are only possible due to the relatively small size of the ISE-CUBE stack (as compared to previous, larger enclosures) and the thin silhouette of the Profiling frame, which limits flow distortion. In addition, the flexibility of the measurement height with the articulating arm is a clear asset for measurements over water surface with strong tidal variation. Finally, it would be quite possible to deploy alongside a tower with fixed height inlets, as these towers have the advantage for automated sampling over much longer time periods. A measurement strategy like this would provide information on the rapidly occurring surface processes alongside the more long-term, continuous context in which they are taking place.

Speculation on such a measurement strategy might imply that the ISE-CUBEs could be deployed for longer periods. However this prototype has a practical time limitation imposed by calibration necessity. Currently, the integrated Cold trap is unsuitable to be used for calibrating CRDS measurements. However, if one could integrate a field calibration module into the system, the system could very likely stand on its own for extended periods of time. While the Analyzer and Pump modules could be used without the Profiling module for an extended deployment, at some duration the benefits of a more conventional enclosure would begin to warrant additional effort during installation. A larger enclosure (such as a pre-existing building) offers a level of security that the ISE-CUBEs cannot provide for long-term measurement efforts that are less concerned with small scale processes; small scale processes which do not necessarily require a long deployment to observe.

Regardless of deployment length, the current ISE-CUBE system is limited by the lack of an active temperature control capability, which presently prevents operation in warmer measurement environments. With the modular approach, the addition of a dedicated ventilation module with larger fans and active cooling/heating unit is straightforward, and would enable deployment in warmer and more variable climatic conditions. Preliminary testing with such a module has already yielded promising results in ambient temperatures up to around $20\,^{\circ}\mathrm{C}$, though shielded from direct sunlight (Sect. 2, Supplemental material).

One potential internal change in our measurement setup would involve the high flow mode described in Sect. 2.2. This mode enabled $4\,\mathrm{Hz}$ sampling and enhanced instrument response time. However, it is unexplored if the measurement precisions found in Sect. 4.2 might be improved if the instrument were to remain in standard low-flow mode. Were this the case, the inlet assembly would need to be modified to even further reduce the amount of tubing subjected to this decreased flow and maintain fast instrument response.

6 Conclusions and Outlook

In this work, we have detailed the design and performance of the new ISE-CUBE system for near-surface profiles of water vapor isotope measurements. The modular design enables rapid installation, while the compact system size provides minimized flow distortion around the measurement site, and allows us to measure in stable conditions with shallow boundary layer.

During a two-week long field experiment in Ny-Ålesund, Svalbard, Norway during Feb–Mar 2020, the analyzer encountered extreme environmental conditions while deployed in the ISE-CUBEs. Though ambient temperatures reached down to $-30\,^{\circ}\mathrm{C}$, the analyzer remained within its specified range of measurement conditions with regard to T_C, T_WB, T_DAS, and p_C. Measurement precisions during the field deployment were on average $0.10\,‰$ ($\delta^{18}\mathrm{O}$) and $0.93\,‰$ ($\delta\mathrm{D}$) lower than in the reference benchmarks.

The profiling module, a height-adjustable sampling arm with a range of $2\,\mathrm{m}$, enabled profiling of the water isotope composition throughout the shallow surface layer in a stable atmosphere. With a response time of approximately $20\,\mathrm{sec}$, the ISE-CUBE system captured profiles and gradients in this layer. Even at the low humidities (down to $0.25\,\mathrm{g/kg}$) over the tundra, the profiles achieve a high enough signal to noise ratio to resolve the vertical isotopic gradients after approximately $4\,\mathrm{minutes}$ at each height interval. Due to the high vertical resolution in the profiles, the observed gradients are robust.

Integration of the Cold-Trapping expansion module based on the design of Peters and Yakir (2010) into the ISE-CUBE system enabled quantitative vapor collection. Samples were typically collected over a duration of 8 hours or more in low-humidity environments, resulting in a maximum collection of $0.3\,\mathrm{mL}$ at a time. Such cold-trapping enables subsequent liquid sample analysis in a laboratory environment for quality control of the calibration, and the measurement of $\mathrm{H_2^{17}O}$ for triple-isotope capability. While the cold trap module is functional, the preliminary results provided here show that design refinements are necessary.

The modular nature of the system invites additional expansion. A top-priority expansion module would focus on an in-field calibration system. In general, there are multiple potential calibration devices using a variety of vapor gen-

eration methods (Iannone et al., 2009; Gkinis et al., 2010; Ellehoj et al., 2013); the device just needs to be robust and suitably compact, all while generating a consistent source of known vapor. For example, Leroy-Dos Santos et al. (2021) have put forward an instrument that can generate stable vapor streams down to $0.045\,\mathrm{g/kg}$ ($70\,\mathrm{ppmv}$), one of which has been operating mostly autonomously in Antarctica, with little manual intervention. Further potential expansion modules include a Battery power module which would permit mobile operation. In addition to an enhanced Ventilation module, an enhanced, automonous Profiling module would remove the need for nearby operators, removing any chance of human-induced error in the stable water isotope measurements.

Deployments need not be limited to measurements of stable water isotopes. Many laser spectrometers for other atmospheric trace gases, such as methane, carbon dioxide, or carbon isotopes may be integrated into the system and used for purposes beyond meteorology/hydrology; those produced by Picarro would most readily fit the system, but are not limited to. With a more robust temperature controller, there is the possibility for deployment in more temperate environments. Such locations may include, but are not limited to, glaciers, sea ice, lakes, coastal areas, caves, forests, grasslands, croplands, deserts, and other places where evaporation and condensation interactions with the surface contribute to the vapor isotope composition of the near-surface atmosphere.

The availability of a modular, versatile deployment system such as the ISE-CUBEs implies easy access to remote locations and environments, while maintaining necessary data quality standards. As we provide the design in a easily reproducible way to the community (see Supplemental Material), we endeavor to enable further development and widespread acquisition of high-quality datasets from previously inaccessible measurement locations.

Appendix A: ISE-CUBE component list

Appendix B: Laboratory benchmark sequences

Appendix C: Profiling module sensor performance

The distance given by the ultrasonic sensor was periodically checked against a manual tape measure throughout the field deployment (accuracy $\pm\sim 2\,\mathrm{cm}$). The behavior of the ultrasonic sensor did vary between the two measurements sites, likely as a result of underlying surface. While deployed over snow, the sensor functioned with $2\,\mathrm{cm}$ accuracy over the range of 50 to $205\,\mathrm{cm}$. When the inlet head was lowered below $50\,\mathrm{cm}$, the sensor gave unreliable and clearly spurious measurements. We speculate that the particular type of ultrasonic sensor used was affected by the acoustic properties of the snowpack below this threshold. In these circumstances, manual distance was taken with a tape measure, with corresponding markings made on the controlling steel cable. No issues with distance sensors were encountered while deployed at the Fjord location with water or sea ice at the surface. At both locations, we observed a low signal to noise ratio and a jumpy distance signal during strong winds ($>11\,\mathrm{m\,s^{-1}}$), possibly due to the ultrasonic pulse being advected away before the reflected signal was received.

The temperature sensor above the tip of the inlet of the profiling module was compared against the temperature sensor of an automated weather station (Jocher et al., 2012; Schulz, 2017) ($20\,\mathrm{m}$ away) at a height of $100\,\mathrm{cm}$ for $37\,\mathrm{hours}$ (during 25 Feb and 26 Feb). The 1-minute averaged temperature records of the two sensors show a high correlation of 0.991, with a linear regression slope of 1.000 ± 0.005 (Figure C1). The profiling sensor consistently recorded higher temperatures than the AWS, having a linear regression offset of $0.6\,^{\circ}\mathrm{C}$. While distance between sensors might account for some of this discrepancy, the gradients observed with the Profiling module are almost an order of magnitude larger, with relative changes well captured due to the high linearity. Overall, the sensors installed on the Profiling module functioned adequately.

Table A1. Components used in the ISE-CUBE system. General gas connections (PTFE tubing, unions, reducers, etc.) made with parts from Swagelok Inc. Files for 3D printed ventilation mounts were custom-made and not listed (see Supplemental Material). Modular abbreviations: AN=Analyzer module; PU=Pump module; CT=Cold Trap module; PR=Profiling module.

Module	Component	Manufacturer	Model/Series	Size(LxWxH); Weight; Detail
AN/PU/CT	Module container	Pelican Products Inc.	iM2875 Storm	632 x 602 x 333 mm; 9.1 kg
AN	CRDS analyser	Picarro Inc.	L-2130i	20.4 kg; 230 VAC
AN/PU	Reinforced PVC vacuum tubing	Kuriyama of America Inc.	K7160-06	3/8 inch
PU	CRDS vacuum pump	KNF DAC GmbH	N920AP.29.18	10.5 kg; 230 VAC
PU	Inlet vacuum pump	KNF DAC GmbH	N022AN.18	4.0 kg; 230 VAC
PU	UPS	Eaton	EL500FR	2.9 kg; 230 VAC
CT	Cryocooler	Sunpower Inc.	Cryotel MT	2.1 kg; 24 VDC
CT	Collection vial	ThermoSci	2-SVW Chromacol	2 mL
CT	UPS	Phoenix Contact	2866611	5.6 kg; 24 VDC
CT	12 VDC (out) power supply	Mean Well	DDR-15G-12	9 to 36 VDC input
CT	Flow meter	Sierra Instruments Inc.	TopTrak 822	12 VDC; 0-1 and 0-30 $\mathrm{L\,min^{-1}}$
AN/PU/CT	Ventilation fan	ebm-papst GmbH & Co. KG	RL 90	0.7 kg; 230 VAC
AN/PU/CT	Protective cover	IKEA	TOSTERÖ	1000 x 700 x 900 mm; 0.75 kg
AN/PU/CT	Power connector	Amphenol	62GB	230 VAC
AN	Data connector	Amphenol	RJ45F7RJ	RJ45
AN/CT	Data connector	RS Pro	111-6759	USB
AN/PU/CT	Inlet vacuum connector	Swagelok Inc.	SS-400-61	1/4 inch
AN/PU	Picarro vacuum connector	Swagelok Inc.	SS-600-61	3/8 inch
AN/PU	One-way check valve	Swagelok Inc.	6L-CW4S4	1/4 inch
PU/CT	Aluminium support frame	RatRig	V-Slot 2020	
CT/PR	Microcontroller	Arduino	UNO and Mega	12 VDC
CT/PR	Temperature sensor	Velleman	VMA324	-55 to 125 °C
PR	Ultrasonic distance sensor	SparkFun Elec.	SEN-15569 (HC-SR04)	0 to 5 m
PR	Module Container	Pelican Products Inc.	1120	214 x 172 x 98 mm; 0.6 kg
PR	Inlet heat trace	Thermon Inc.	BSX 10-2	60 °C; 32 W/m
PR	Aluminium tripod	Campbell Scientific	CM110	15 kg
PR	Hand winch	Hamron	-	350 kg rating
AN/PU/CT	AC mains power cable	Lapp	0013631	3-core; 230 V; -40 °C rating
PU/PR	DC power and signal cable	Alpha Wire EcoFlex	79002 SL005	3-core; 12 V; -40 °C rating

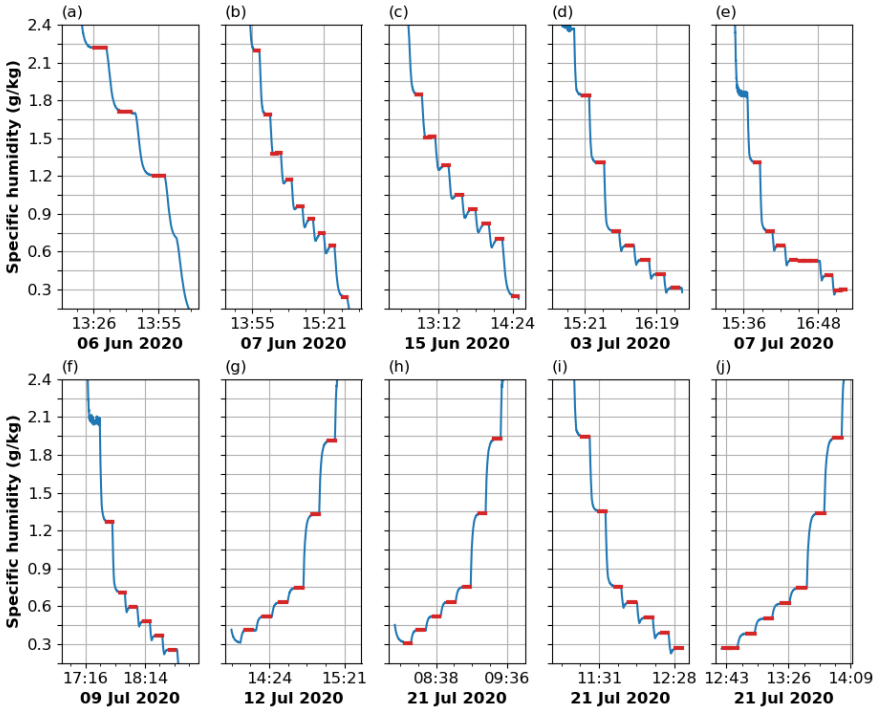

Figure B1. Humidity step sequences from ten (a-j) distinct usage events from laboratory characterization of the analyzer, during the period of June to July 2020. Blue line depicts volumetric mixing ratio, with red highlights showing $5\,\mathrm{minute}$ periods with a standard deviation less than $0.006\,\mathrm{g/kg}$. (a-c) used $100\,\%$ nitrogen as carrier gas, while (d-j) used synthetic air ($80\,\%$ N_2, $20\,\%$ O_2). All events used a lab standard of a similar depletion (δ^{18}O: $-40.02 \pm 0.07\,‰$ and δD: $-307.8 \pm 0.8\,‰$) as measured in the field.

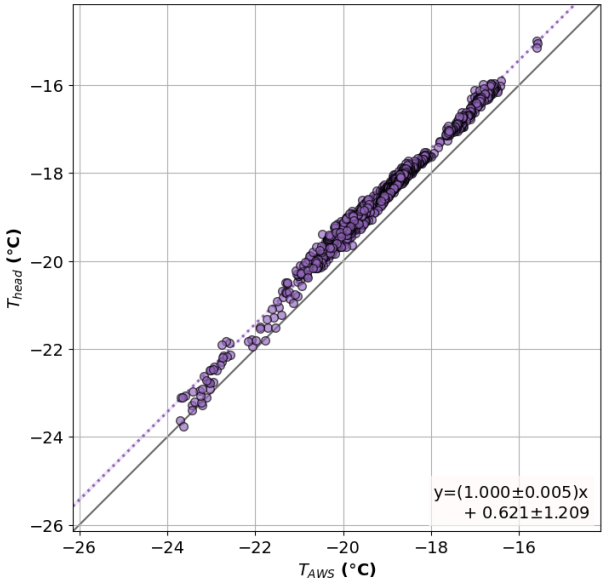

Figure C1. Comparison between temperature sensor of automated weather station (T_{AWS}) and the inlet temperature sensor (T_{head}). Both were at a height of 100 cm above the surface of the snow for 37 hours. Solid gray line represents 1-to-1 ratio. Dotted line indicates linear regressions through the data points, with purple shading (barely visible under dotted line) shows the 95 % confidence interval.

Data availability. The data shown in this paper are available upon request from the corresponding author.

Author contributions. Conceptualization (design): AS, HS, HCSL; Methodology (construction): AS, HS; Investigation: AS, HS; Formal analysis: AS, HS; Writing – original draft preparation: AS; Writing – review and editing: All authors

Competing interests. The authors declare no conflict of interest. The funders had no role in the design of the study; in the collection, analyses, or interpretation of data; in the writing of the manuscript, or in the decision to publish the results.

Acknowledgements. The authors wish to acknowledge: Anak Bhandari, Helge Bryhni, Tor de Lange, Aina Johannessen, Alena Dekhtyareva, Marius Jonassen, and Daniele Zannoni for their help and assistance in this project; Alexander Schulz for the data from the AWI Ny-Ålesund eddy-covariance meteorological station; and Ove Hermansen for access to Zeppelin Observatory. Finally, we express our gratitude to Neils Munksgaard and three anonymous referees for their constructive comments and suggestions to improve this manuscript during the review process. The authors also wish to make a special acknowledgment to the memory of Leon Isaac Peters for his incredibly patient and supportive insights regarding the design of the Cold Trap module. This work has been funded by the European Research Council (Consolidator Grant ISLAS, project. 773245).

References

Aemisegger, F., Sturm, P., Graf, P., Sodemann, H., Pfahl, S., Knohl, A., and Wernli, H.: Measuring variations of δ18O and δ2H in atmospheric water vapour using two commercial laser-based spectrometers: an instrument characterisation study, Atmospheric Measurement Techniques, 5, 1491–1511, https://doi.org/10.5194/amt-5-1491-2012, https://amt.copernicus.org/articles/5/1491/2012/, 2012.

Bonne, J. L., Masson-Delmotte, V., Cattani, O., Delmotte, M., Risi, C., Sodemann, H., and Steen-Larsen, H. C.: The isotopic composition of water vapour and precipitation in Ivittuut, southern Greenland, Atmospheric Chemistry and Physics, 14, 4419–4439, https://doi.org/10.5194/acp-14-4419-2014, 2014.

Chazette, P., Flamant, C., Sodemann, H., Totems, J., Monod, A., Dieudonné, E., Baron, A., Seidl, A., Steen-Larsen, H. C., Doira, P., Durand, A., and Ravier, S.: Experimental investigation of the stable water isotope distribution in an Alpine lake environment (L-WAIVE), Atmospheric Chemistry and Physics, 21, 10 911–10 937, https://doi.org/10.5194/acp-21-10911-2021, 2021.

Craig, H.: Isotopic Variations in Meteoric Waters, Science, 133, 1702–1703, 1961.

Crosson, E. R.: A cavity ring-down analyzer for measuring atmospheric levels of methane, carbon dioxide, and water vapor, Applied Physics B: Lasers and Optics, 92, 403–408, https://doi.org/10.1007/s00340-008-3135-y, 2008.

Crosson, E. R., Ricci, K. N., Richman, B. A., Chilese, F. C., Owano, T. G., Provencal, R. A., Todd, M. W., Glasser, J., Kachanov, A. A., Paldus, B. A., Spence, T. G., and Zare, R. N.: Stable Isotope Ratios Using Cavity Ring-Down Spectroscopy: Determination of 13C/12C for Carbon Dioxide in Human Breath, Analytical Chemistry, 74, 2003–2007, https://doi.org/10.1021/ac025511d, https://doi.org/10.1021/ac025511d, pMID: 12033299, 2002.

Dahlke, S., Solbès, A., and Maturilli, M.: Cold Air Outbreaks in Fram Strait: Climatology, Trends, and Observations During an Extreme Season in 2020, Journal of Geophysical Research: Atmospheres, 127, 1–18, https://doi.org/10.1029/2021JD035741, https://onlinelibrary.wiley.com/doi/10.1029/2021JD035741, 2022.

Ellehoj, M. D., Steen-Larsen, H. C., Johnsen, S. J., and Madsen, M. B.: Ice-vapor equilibrium fractionation factor of hydrogen and oxygen isotopes: Experimental investigations and implications for stable water isotope studies, Rapid Communications in Mass Spectrometry, 27, 2149–2158, https://doi.org/10.1002/rcm.6668, http://doi.wiley.com/10.1002/rcm.6668, 2013.

Galewsky, J., Rella, C., Sharp, Z., Samuels, K., and Ward, D.: Surface measurements of upper tropospheric water vapor isotopic composition on the Chajnantor Plateau, Chile, Geophysical Research Letters, 38, 1–5, https://doi.org/10.1029/2011GL048557, 2011.

Galewsky, J., Steen-Larsen, H. C., Field, R. D., Worden, J., Risi, C., and Schneider, M.: Stable isotopes in atmospheric water vapor and applications to the hydrologic cycle, Reviews of Geophysics, 54, 809–865, https://doi.org/10.1002/2015RG000512, 2016.

Gkinis, V., Popp, T. J., Johnsen, S. J., and Blunier, T.: A continuous stream flash evaporator for the calibration of an IR cavity ring-down spectrometer for the isotopic analysis of water cavity ring-down spectrometer for the isotopic analysis of water, Isotopes in Environmental and Health Studies, 46, 463–475, https://doi.org/https://doi.org/10.1080/10256016.2010.538052, 2010.

Gupta, P., Noone, D., Galewsky, J., Sweeney, C., and Vaughn, B. H.: Demonstration of high-precision continuous measurements of water vapor isotopologues in laboratory and remote field deployments using wavelength-scanned cavity ring-down spectroscopy (WS-CRDS) technology, Rapid Communications in Mass Spectrometry, 23, 2534–2542, https://doi.org/10.1002/rcm.4100, http://doi.wiley.com/10.1002/rcm.4100, 2009.

Iannone, R. Q., Romanini, D., Kassi, S., Meijer, H. A. J., and Kerstel, E.: A Microdrop Generator for the Calibration of a Water Vapor Isotope Ratio Spectrometer, Journal of Atmospheric and Oceanic Technology, 26, 1275–1288, https://doi.org/10.1175/2008JTECHA1218.1, 2009.

Jocher, G., Karner, F., Ritter, C., Neuber, R., Dethloff, K., Obleitner, F., Reuder, J., and Foken, T.: The Near-Surface Small-Scale Spatial and Temporal Variability of Sensible and Latent Heat Exchange in the Svalbard Region: A Case Study, ISRN Meteorology, 2012, 1–14, https://doi.org/10.5402/2012/357925, https://www.hindawi.com/journals/isrn/2012/357925/, 2012.

Johnson, J. E. and Rella, C. W.: Effects of variation in background mixing ratios of N2, O2, and Ar on the measurement of δ18O–H2O and δ2H–H2O values by cavity ring-down spectroscopy, Atmospheric Measurement Techniques, 10,

3073–3091, https://doi.org/10.5194/amt-10-3073-2017, https://amt.copernicus.org/articles/10/3073/2017/, 2017.

Leroy-Dos Santos, C., Casado, M., Prié, F., Jossoud, O., Kerstel, E., Farradèche, M., Kassi, S., Fourré, E., and Landais, A.: A dedicated robust instrument for water vapor generation at low humidity for use with a laser water isotope analyzer in cold and dry polar regions, Atmospheric Measurement Techniques, 14, 2907–2918, https://doi.org/10.5194/amt-14-2907-2021, https://amt.copernicus.org/articles/14/2907/2021/, 2021.

Mahrt, L.: Stably Stratified Atmospheric Boundary Layers, Annual Review of Fluid Mechanics, 46, 23–45, https://doi.org/10.1146/annurev-fluid-010313-141354, https://www.annualreviews.org/doi/10.1146/annurev-fluid-010313-141354, 2014.

Massman, W. J. and Ibrom, A.: Attenuation of concentration fluctuations of water vapor and other trace gases in turbulent tube flow, Atmospheric Chemistry and Physics, 8, 6245–6259, https://doi.org/10.5194/acp-8-6245-2008, https://acp.copernicus.org/articles/8/6245/2008/, 2008.

Munksgaard, N. C., Wurster, C. M., and Bird, M. I.: Continuous analysis of δ 18O and δD values of water by diffusion sampling cavity ring-down spectrometry: A novel sampling device for unattended field monitoring of precipitation, ground and surface waters, Rapid Communications in Mass Spectrometry, 25, 3706–3712, https://doi.org/10.1002/rcm.5282, 2011.

Munksgaard, N. C., Wurster, C. M., Bass, A., Zagorskis, I., and Bird, M. I.: First continuous shipboard δ 18O and δD measurements in sea water by diffusion sampling-cavity ring-down spectrometry, Environmental Chemistry Letters, 10, 301–307, https://doi.org/10.1007/s10311-012-0371-5, 2012.

Papritz, L. and Spengler, T.: A Lagrangian Climatology of Wintertime Cold Air Outbreaks in the Irminger and Nordic Seas and Their Role in Shaping Air–Sea Heat Fluxes, Journal of Climate, 30, 2717–2737, https://doi.org/10.1175/JCLI-D-16-0605.1, http://journals.ametsoc.org/doi/10.1175/JCLI-D-16-0605.1, 2017.

Peters, L. I. and Yakir, D.: A rapid method for the sampling of atmospheric water vapour for isotopic analysis, Rapid Communications in Mass Spectrometry, 24, 103–108, https://doi.org/10.1002/rcm.4359, http://doi.wiley.com/10.1002/rcm.4359, 2010.

Picarro Inc.: L2140-i, L2130-i or L2120-i Analyzer and Peripherals: Operation, Maintenance, and Troubleshooting User's Manual - 40035, 2013.

Picarro Inc.: L2130-i Analyzer Datasheet, 2021.

Ritter, F., Steen-Larsen, H. C., Werner, M., Masson-Delmotte, V., Orsi, A., Behrens, M., Birnbaum, G., Freitag, J., Risi, C., and Kipfstuhl, S.: Isotopic exchange on the diurnal scale between near-surface snow and lower atmospheric water vapor at Kohnen station, East Antarctica, The Cryosphere, 10, 1647–1663, https://doi.org/10.5194/tc-10-1647-2016, https://tc.copernicus.org/articles/10/1647/2016/, 2016.

Schulz, A.: Untersuchung der Wechselwirkung synoptisch-skaliger mit orographisch bedingten Prozessen in der arktischen Grenzschicht über Spitzbergen, Monograph, Universität Potsdam, https://publishup.uni-potsdam.de/frontdoor/index/index/docId/40005, 2017.

Sodemann, H., Aemisegger, F., Pfahl, S., Bitter, M., Corsmeier, U., Feuerle, T., Graf, P., Hankers, R., Hsiao, G., Schulz, H., Wieser, A., and Wernli, H.: The stable isotopic composition of water vapour above Corsica during the HyMeX SOP1 campaign: Insight into vertical mixing processes from lower-tropospheric survey flights, Atmospheric Chemistry and Physics, 17, 6125–6151, https://doi.org/10.5194/acp-17-6125-2017, 2017.

Steen-Larsen, H. C., Johnsen, S. J., Masson-Delmotte, V., Stenni, B., Risi, C., Sodemann, H., Balslev-Clausen, D., Blunier, T., Dahl-Jensen, D., Ellehøj, M. D., Falourd, S., Grindsted, A., Gkinis, V., Jouzel, J., Popp, T., Sheldon, S., Simonsen, S. B., Sjolte, J., Steffensen, J. P., Sperlich, P., Sveinbjörnsdóttir, A. E., Vinther, B. M., and White, J. W.: Continuous monitoring of summer surface water vapor isotopic composition above the Greenland Ice Sheet, Atmospheric Chemistry and Physics, 13, 4815–4828, https://doi.org/10.5194/acp-13-4815-2013, 2013.

Steen-Larsen, H. C., Sveinbjörnsdottir, A. E., Peters, A. J., Masson-Delmotte, V., Guishard, M. P., Hsiao, G., Jouzel, J., Noone, D., Warren, J. K., and White, J. W. C.: Climatic controls on water vapor deuterium excess in the marine boundary layer of the North Atlantic based on 500 days of in situ, continuous measurements, Atmospheric Chemistry and Physics, 14, 7741–7756, https://doi.org/10.5194/acp-14-7741-2014, https://acp.copernicus.org/articles/14/7741/2014/, 2014.

Steig, E. J., Gkinis, V., Schauer, A. J., Schoenemann, S. W., Samek, K., Hoffnagle, J., Dennis, K. J., and Tan, S. M.: Calibrated high-precision 17O-excess measurements using cavity ring-down spectroscopy with laser-current-tuned cavity resonance, Atmospheric Measurement Techniques, 7, 2421–2435, https://doi.org/10.5194/amt-7-2421-2014, 2014.

Thurnherr, I., Hartmuth, K., Jansing, L., Gehring, J., Boettcher, M., Gorodetskaya, I., Werner, M., Wernli, H., and Aemisegger, F.: The role of air–sea fluxes for the water vapour isotope signals in the cold and warm sectors of extratropical cyclones over the Southern Ocean, Weather and Climate Dynamics, 2, 331–357, https://doi.org/10.5194/wcd-2-331-2021, https://wcd.copernicus.org/articles/2/331/2021/, 2021.

Wahl, S., Steen-Larsen, H. C., Reuder, J., and Hörhold, M.: Quantifying the Stable Water Isotopologue Exchange Between the Snow Surface and Lower Atmosphere by Direct Flux Measurements, Journal of Geophysical Research: Atmospheres, 126, 1–24, https://doi.org/10.1029/2020JD034400, https://onlinelibrary.wiley.com/doi/10.1029/2020JD034400, 2021.

Weng, Y., Touzeau, A., and Sodemann, H.: Correcting the impact of the isotope composition on the mixing ratio dependency of water vapour isotope measurements with cavity ring-down spectrometers, Atmospheric Measurement Techniques, 13, 3167–3190, https://doi.org/10.5194/amt-13-3167-2020, https://amt.copernicus.org/articles/13/3167/2020/, 2020.

Zeeman, M. J., Selker, J. S., and Thomas, C. K.: Near-Surface Motion in the Nocturnal, Stable Boundary Layer Observed with Fibre-Optic Distributed Temperature Sensing, Boundary-Layer Meteorology, 154, 189–205, https://doi.org/10.1007/s10546-014-9972-9, http://link.springer.com/10.1007/s10546-014-9972-9, 2015.